



This is a repository copy of *Fabrication of hierarchically porous trabecular bone replicas via 3D printing with high internal phase emulsions (HIPEs)*.

White Rose Research Online URL for this paper:

<https://eprints.whiterose.ac.uk/219447/>

Version: Published Version

---

**Article:**

Sengokmen-Ozsoz, N. [orcid.org/0000-0002-2000-7408](https://orcid.org/0000-0002-2000-7408), Aleemardani, M. [orcid.org/0000-0001-8261-4046](https://orcid.org/0000-0001-8261-4046), Palanca, M. [orcid.org/0000-0002-1231-2728](https://orcid.org/0000-0002-1231-2728) et al. (4 more authors) (2024) Fabrication of hierarchically porous trabecular bone replicas via 3D printing with high internal phase emulsions (HIPEs). *Biofabrication*, 17 (1). ISSN 1758-5082

<https://doi.org/10.1088/1758-5090/ad8b70>

---

**Reuse**

This article is distributed under the terms of the Creative Commons Attribution (CC BY) licence. This licence allows you to distribute, remix, tweak, and build upon the work, even commercially, as long as you credit the authors for the original work. More information and the full terms of the licence here:

<https://creativecommons.org/licenses/>

**Takedown**

If you consider content in White Rose Research Online to be in breach of UK law, please notify us by emailing [eprints@whiterose.ac.uk](mailto:eprints@whiterose.ac.uk) including the URL of the record and the reason for the withdrawal request.



[eprints@whiterose.ac.uk](mailto:eprints@whiterose.ac.uk)  
<https://eprints.whiterose.ac.uk/>



PAPER • OPEN ACCESS

# Fabrication of hierarchically porous trabecular bone replicas via 3D printing with high internal phase emulsions (HIPEs)

To cite this article: Nihan Sengokmen-Ozsoz *et al* 2025 *Biofabrication* **17** 015012

View the [article online](#) for updates and enhancements.

## You may also like

- [Chlorella-enriched hydrogels protect against myocardial damage and reactive oxygen species production in an \*in vitro\* ischemia/reperfusion model using cardiac spheroids](#)  
Martine Tarsitano, Clara Liu Chung Ming, Lucia Bennar *et al.*
- [On-chip human lymph node stromal network for evaluating dendritic cell and T-cell trafficking](#)  
Brian J Kwee, Mona Mansouri, Adovi Akue *et al.*
- [Standalone single- and bi-layered human skin 3D models supported by recombinant silk feature native spatial organization](#)  
Savvini Gkouma, Nayanika Bhalla, Solène Frapard *et al.*

# Biofabrication



## PAPER

### OPEN ACCESS

RECEIVED  
18 June 2024

REVISED  
20 September 2024

ACCEPTED FOR PUBLICATION  
25 October 2024







PUBLISHED  
4 November 2024

Original content from this work may be used under the terms of the [Creative Commons Attribution 4.0 licence](#).

Any further distribution of this work must maintain attribution to the author(s) and the title of the work, journal citation and DOI.



# Fabrication of hierarchically porous trabecular bone replicas via 3D printing with high internal phase emulsions (HIPEs)

Nihan Sengokmen-Ozsoz<sup>1,2,8</sup> , Mina Aleemardani<sup>1,3,8</sup> , Marco Palanca<sup>4,5,6</sup> , Alice Hann<sup>7</sup>, Gwendolen C Reilly<sup>7</sup> , Enrico Dall'Ara<sup>4,5</sup>  and Frederik Claeysens<sup>1,\*</sup> 

<sup>1</sup> Kroto Research Institute, Department of Materials Science and Engineering, The University of Sheffield, Sheffield S3 7HQ, United Kingdom

<sup>2</sup> Department of Materials Science and Engineering, Gebze Technical University, Gebze, Kocaeli 41400, Turkey

<sup>3</sup> Department of Translational Health Science, Bristol Medical School, University of Bristol, Bristol BS1 3NY, United Kingdom

<sup>4</sup> Department of Oncology and Metabolism, The University of Sheffield, Sheffield, United Kingdom

<sup>5</sup> INSIGNEO Institute for In Silico Medicine, The University of Sheffield, Sheffield, United Kingdom

<sup>6</sup> Department of Industrial Engineering, Alma Mater Studiorum—University of Bologna, Bologna, Italy

<sup>7</sup> Department of Materials Science and Engineering, Pam Liversidge Building, Mappin Street, Sheffield, United Kingdom

<sup>8</sup> Contributed equally to this work as joint first authors.

\* Author to whom any correspondence should be addressed.

E-mail: [f.claeysens@sheffield.ac.uk](mailto:f.claeysens@sheffield.ac.uk)

**Keywords:** additive manufacturing, 3D printing, polyHIPEs, porous scaffolds, trabecular bone

Supplementary material for this article is available [online](#)

## Abstract

Combining emulsion templating with additive manufacturing enables the production of inherently porous scaffolds with multiscale porosity. This approach incorporates interconnected porous materials, providing a structure that supports cell ingrowth. However, 3D printing hierarchical porous structures that combine semi-micropores and micropores remains a challenging task. Previous studies have demonstrated that using a carefully adjusted combination of light absorbers and photoinitiators in the resin can produce open surface porosity, sponge-like internal structures, and a printing resolution of about 150  $\mu\text{m}$ . In this study, we explored how varying concentrations of tartrazine (0, 0.02, 0.04, and 0.08 wt%) as a light absorber affect the porous structure of acrylate-based polymerized medium internal phase emulsions fabricated via vat photopolymerization. Given the importance of a porous and interconnected structure for tissue engineering and regenerative medicine, we tested cell behavior on these 3D-printed disk samples using MG-63 cells, examining metabolic activity, adhesion, and morphology. The 0.08 wt% tartrazine-containing 3D-printed sample (008 T) demonstrated the best cell proliferation and adhesion. To show that this high internal phase emulsion (HIPE) resin can be used to create complex structures for biomedical applications, we 3D-printed trabecular bone structures based on microCT imaging. These structures were further evaluated for cell behavior and migration, followed by microCT analysis after 60 days of cell culture. This research demonstrates that HIPEs can be used as a resin to print trabecular bone mimics using additive manufacturing, which could be further developed for lab-on-a-chip models of healthy and diseased bone.

## 1. Introduction

Emulsion templating is a versatile method to produce porous polymers as it enables the production of interconnected porosity. The process involves creating an emulsion by mixing a typically hydrophobic monomer mixture (continuous phase) with water as a dispersed phase (internal phase) and a suitable surfactant [1–9] or particles [10, 11]. This results in

a suspension of water droplets surrounded by a continuous monomer phase. When the internal phase exceeds 74% of the total volume (TV), it is classified as a high internal phase emulsion (HIPE). By polymerizing the continuous phase through cross-linking the continuous monomer phase, the three-dimensional (3D) structure of the emulsion is preserved, and the water is removed, resulting in a polymerized HIPE (PolyHIPE) scaffold [12]. The

morphology of the polyHIPEs can be easily controlled by adjusting parameters such as the volume of the internal phase, the addition of different additives, temperature, stirring speed, surface functionalization with hydrophilic molecules, or plasma treatment [13, 14].

Various types of polyHIPEs have been used in tissue engineering, including styrene-based, thiol-ene-based, polyester-based, polysaccharide-based, and acrylate-based polyHIPEs [15]. Each type offers distinct advantages and properties for tissue engineering applications. Styrene-based polyHIPEs support 3D cell culture and have demonstrated superior cell growth, viability, and cytotoxic tolerance compared to standard two-dimensional cell culture on tissue culture plastic (TCP) [16, 17]. This resulted in the development of a commercially available polystyrene-based polyHIPE called Alvetex which is commonly used for 3D cell culture [18]. Functionalization of these substrates with biological molecules like hyaluronic acid (HA), poly-D-lysine, or laminin can modify the surface properties of these 3D environments and promote specific cell functions [19, 20]. Although these styrene-based scaffolds are inherently non-degradable, which makes them less suitable for tissue engineering they show excellent potential for 3D tissue growth environments [15]. Recently, there have been a number of approaches to produce biodegradable polyHIPEs. For example, thiol-ene-based polyHIPEs offer good mechanical properties and support cell proliferation and cartilage growth [21]. By functionalizing them with molecules like sulfonate groups or maleimide, cell attachment and proliferation can be enhanced [22, 23]. Incorporating biodegradable polycaprolactone (PCL) into thiol-ene scaffolds allows for hydrolysis and the production of non-toxic compounds [24]. Polyester-based polyHIPEs, such as poly( $\epsilon$ -caprolactone) PCL and poly( $\epsilon$ -caprolactone urethane) PCLU, demonstrate biodegradability while supporting cell growth and enabling drug release [4, 25, 26]. Molecules like hydroxyapatite (HA) further enhance their properties [27, 28]. Polysaccharide-based polyHIPEs derived from natural polysaccharides offer advantages for scaffold synthesis, providing an extracellular matrix-like environment for cell growth [29, 30]. These scaffolds can be produced through various crosslinking methods and exhibit improved cell loading efficiency and viability [31].

PolyHIPEs can be shaped using traditional manufacturing techniques like casting or molding to create structures with low design complexity and flexibility [32, 33]. Post-processing can also be applied to create more intricate structures. A novel approach involves combining emulsion templating with additive manufacturing, enabling the one-step production of inherently porous and lightweight complex structures with little to none post-processing [13, 34]. This approach

allows for the production of porous scaffolds with multiscale porosity [13]. Additive manufacturing techniques such as material extrusion (fused deposition modeling) and vat photopolymerization (stereolithography, SLA) are utilized for manufacturing polymer materials and have been employed to construct porous polyHIPE 3D structures [13, 34, 35]. In previous studies, experimental in-house setups were utilized to print bespoke emulsions prepared by combining water with appropriate monomers, surfactants, crosslinkers, and photoinitiators [1, 3, 13]. The printability of these emulsions in commercial stereolithography-based 3D printers were investigated for the first time in our previous work [36].

Although additive manufacturing allows for the production of complex polyHIPE structures, HIPE-based resins scatter light during the 3D printing process, resulting in poorly defined and low-resolution structures [13]. Previous research has explored the application of light absorbers as a viable solution to address this issue, resulting in notable resolution enhancement in both traditional non-porous stereolithography resins [37] and emulsion-based resins [13]. The main purpose of using light absorbers is to absorb excess light, prevent light scattering, and restrict the photopolymerization of resins to the intended shapes and sizes. Without appropriate light absorbers, the accuracy of 3D printing for photosensitive resins is significantly limited. To date, various light absorbers, as listed in table 1, have been employed to enhance 3D printing resolution and achieve the desired shape fidelity. For example, Tinuvin 234 has been utilized as a light absorber to increase resolution in HIPE-based resins, minimizing light scattering and improving printing quality. Without light absorbers, the surfaces of structures may become non-porous due to inadequate curing of the polymer in the scattering region. This surface skin reduces the functionality of the structures, particularly in applications where surface porosity is essential, such as cell culture scaffolds [13].

In previous studies, we demonstrated excellent correspondence between the .stl file and the printed structures in replicating complex geometries. We initially utilized these emulsions in an in-house built stereolithography setup to print woodpile structures [13], followed by the use of a commercial 3D printer to optimize the emulsion for fabricating inherently porous, complex structures [36]. Additionally, a more cost-effective commercial 3D printer was employed to produce regular lattice structures [38]. Our previous work has demonstrated the use of beta-carotene and tartrazine as light absorbers has improved the printing resolution of the same composition of acrylate-based polymerized medium internal phase emulsions (polyMIPEs) used in this study, while tartrazine has provided open surface porosity [36]. Open surface porosity can be useful in biomedical applications, as

**Table 1.** Examples of the previously used light absorbers in 3D printing of polymers.

Light absorber	Polymer matrix	3D printing technique	Reported advantages of using light absorber
Tinuvin <sup>®</sup> 327	The photocurable prepolymer was mainly composed of isobornyl acrylate (IBXA), 1,6-hexanediol diacrylate (HDDA), and bisphenol-A-ethoxylated (4) diacrylate (BEDA).	In-house built dynamic mask projection microstereolithography set-up	Improved shape fidelity and geometric accuracy of microstructures in particular with overhanging features [37].
Tinuvin <sup>®</sup> 234	The emulsion was mainly composed of water, isobornyl acrylate (IBOA) and (trimethylolpropane triacrylate (TMPTA).	In house-built stereolithography setup	Improved the printing resolution of PolyHIPEs [13].
Carbon nanotube	The commercially available high-ceramic-yield polysilazane preceramic polymer (PSZ, Eisen Technology, China)	DLP-based 3D printer (Hanhai Technology, Wuxi, China)	Effective control of photocuring thickness and improved printing precision [50].
Cyasorb <sup>®</sup> UV 416, Tinuvin <sup>®</sup> 327, and Chiguard <sup>®</sup> 323	ORMOCER <sup>®</sup> -based resin.	DLP-based 3D printer (S60 LED machine, Rapidshape, Germany)	Improved geometrical accuracy of 3D-printed parts [51].
2,5-bis(5-tert-butyl-2-benzoxazolyl) thiophene	The resin was mainly composed of epoxy acrylate, Hexamethylene diacrylate, and trimethylolpropane triacrylate (TMPTA).	DLP-based 3D printer (Advanced Micro, Nanjing Micro quick Co., Ltd)	Improved the printing resolution of 3D printed parts [52].
Tartrazine	The photosensitive gel ink was mainly composed of Acrylamide (AM) and methylenebisacrylamide (MBAA).	DLP-based 3D printer (Creality LD006, China)	Maintained a good printing fidelity reducing excessive polymerization [53].
Sudan I	PEG-bisurethane methacrylate (PEG-BUM).	SLA 3D printer	Allowed controlling the resolution of the printed structures and enabled the printing of more complex geometries that include over-hanging features [54].
Beta carotene and Tartrazine	The emulsion was mainly composed of water, 2-ethylhexyl acrylate (EHA), isobornyl acrylate (IBOA) and (trimethylolpropane triacrylate (TMPTA).	DLP-based 3D printer (Kudo 3D Titan2 HR)	Improved the printing resolution and shape fidelity of PolyHIPEs [36].

it promotes cell attachment. Therefore, the primary goal of this study is to explore this effect and its impact on cell behavior.

Tissue engineering is a multidisciplinary approach aimed at enhancing or replacing biological tissues. Porous structures/scaffolds are essential in tissue engineering as they simulate the natural extracellular matrix, offering an ideal environment for cell growth and tissue repair. Their interconnected pores facilitate cell movement, nutrient and oxygen delivery, and waste removal. This design can promote new blood vessel formation, which is vital for tissue survival. Additionally, these scaffolds provide the

right balance of strength and flexibility, mimicking natural tissues and allowing controlled degradation and replacement. By customizing pore size and distribution, porous scaffolds enhance the integration and functionality of engineered tissues, supporting effective regeneration [39–41].

Trabecular bone, also referred to as spongy bone, is a type of bone tissue known for its porous and lattice-like structure [42]. It is one of the primary types of bone tissue present in the human skeleton, alongside cortical bone [43]. Trabecular bone is composed of interconnected bony struts called trabeculae, which form a 3D heterogeneous lattice [42].

This lattice provides strength and support to the bone while keeping it lightweight [44]. Trabecular bone is highly vascularized, enabling the exchange of nutrients and waste products [45]. It is particularly responsive to changes in mechanical loading and plays a role in absorbing and redistributing forces during weight-bearing activities [46]. Due to its hierarchical structure, different porosities can be found in the trabecular bone. The space between trabeculae (in the order of 300–1000  $\mu\text{m}$ ) is filled with bone marrow, blood vessels and nerves. However, in the mineralized portion of the bone (i.e. the trabeculae) micro-porosities such as osteocyte lacunae (which host the osteocytes, bone cells in the order of 10  $\mu\text{m}$  in size) and nanoporosities such as canaliculi (which host the osteocytes' dendritic processes, in the order of a few 100 nm) can be observed. One technique for creating trabecular bone is decellularization, but it comes with several challenges. These include the limited availability of trabecular bone sources, difficulties in controlling its composition and structure, and potential issues like disease transfer, structural damage, and changes to the bone's mechanical properties. Since trabecular bone has a highly complex structure, 3D printing is often needed to achieve the high resolution required for intricate designs. Overall, replicating the structure and function of trabecular bone is challenging due to problems with accurately mimicking its natural architecture, providing an appropriate environment for cell growth and differentiation, and ensuring the right mechanical properties [47–49]. Since trabecular bone is highly porous with pores ranging from nano to micro sizes, this structure can be more accurately replicated using a naturally porous resin, like HIPEs.

In this study, we examined the effect of different tartrazine concentrations (0, 0.02, 0.04, and 0.08 wt%) as a light absorber in acrylate-based polyMIPEs (scheme 1). The prepared HIPEs with varying tartrazine concentrations were 3D-printed using an Elegoo Mars 3 Pro, producing polyMIPE disks, and the impact of tartrazine concentration on their porosity was analyzed. Given their porous and interconnected structure, these 3D-printed polyMIPEs are well-suited for biomedical applications. Cell behavior was tested using MG-63 cells on the disks, and the 0.08 wt% tartrazine disk (labeled 008 T) demonstrated the highest cell metabolic activity, attachment and ALP activity, making it the optimal choice. To showcase the potential of this HIPE for fabricating complex structures through vat photopolymerization for tissue engineering, we 3D-printed a human trabecular bone structure based on microCT imaging (scheme 1). The 3D-printed trabecular bone structures were then seeded with MG-63 cells, which showed effective attachment and migration. These structures featured a range of pore sizes with distributed and interconnected porosity, promoting cell

migration, penetration, and nutrient diffusion, and closely mimicked natural bone.

## 2. Materials and methods

2-ethylhexyl acrylate (EHA), isobornyl acrylate (IBOA), trimethylolpropane triacrylate (TMPTA), a photoinitiator; diphenyl (2,4,6-trimethyl benzoyl)-phosphine oxide/2-hydroxy-2-methyl propiophenone (blend), and tartrazine (dye content  $\geq 85\%$ ), were all purchased from Sigma Aldrich. The surfactant Hypermer B246-SO-M was kindly donated by Croda.

### 2.1. Preparation of HIPEs

The continuous organic phase was prepared by mixing 39.70 wt% of EHA, 39.70 wt% of IBOA, 15.90 wt% of TMPTA (crosslinker), and 4.70 wt% of Hypermer B246-SO-M as a surfactant (table 2). The mixture was heated to 50 °C to completely dissolve the surfactant within it. To act as a light absorber, tartrazine was incorporated into the continuous organic phase at 0.02 wt%, 0.04 wt%, and 0.08 wt% relative to the overall mixture. Following that, the photoinitiator was added to the continuous phase at 5 wt%. Finally, the emulsion was formed by slowly adding 80 vol% of distilled water ( $\text{dH}_2\text{O}$ ) as the internal phase to the mixture while stirring at a speed of 300 rpm (SciQuip-Pro 40 stirrer).

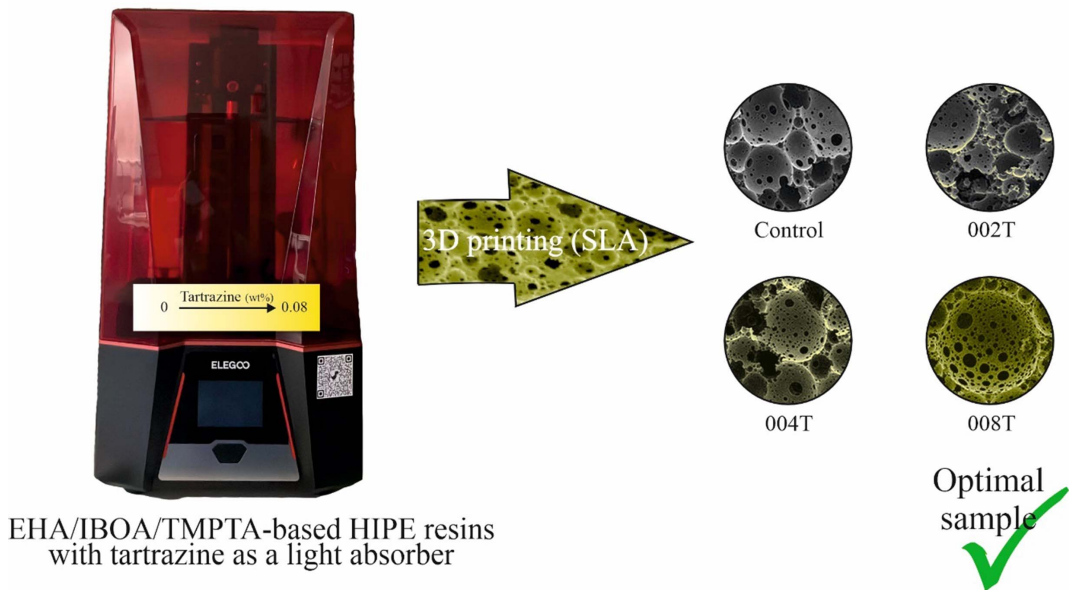
### 2.2. 3D printing of polyHIPE disks and trabecular structures

PolyHIPE structures were fabricated using a commercial 3D printer (Elegoo Mars 3pro) that operates on the principles of stereolithography (SLA). The printer utilizes a high-resolution 4 K monochrome LCD screen with dimensions of 4098  $\times$  2560 pixels and an XY resolution of 35  $\mu\text{m}$ . Additionally, it incorporates a chip-on-board lens equipped with integrated UV LED lights and a Fresnel lens, enabling the emission of a uniform 405 nm light beam for the printing process [55].

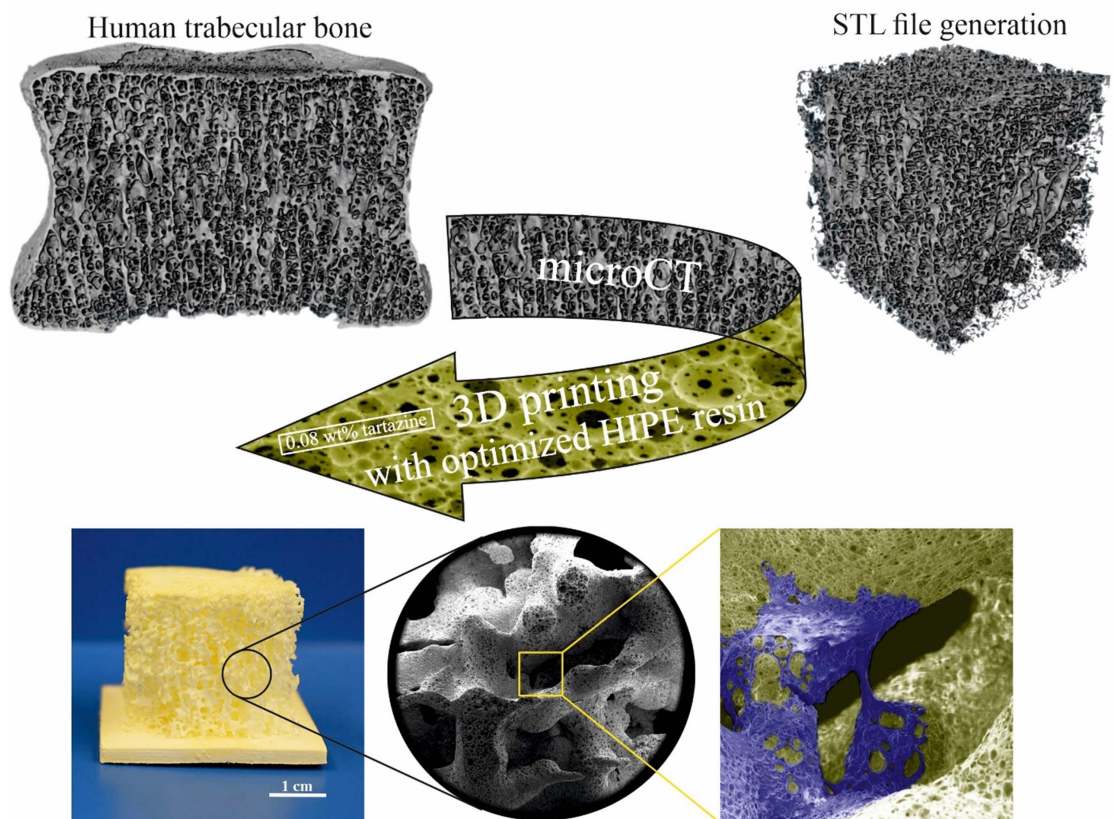
Computer-aided design was used to prepare a 9 mm diameter  $\times$  1 mm height disk for cell culture activities and 10 mm diameter  $\times$  2.5 mm height disk for the characterization (SolidWorks 2018).

Trabecular bone structure was obtained from a human vertebra, following protocols approved by the Bioethics Committee of the University of Bologna (reference n. 17325, 8 February 2019) and of The University of Sheffield (reference n. 031782, 22 June 2020). Briefly, the L3 vertebral body of a donor (Caucasian, female, 51 years old) was scanned with micro-computed tomography (VivaCT80, Scanco Medical Ltd, Switzerland) with the following scanning parameters: current: 114 mA, voltage: 70 kVp, integration time: 300 ms, power: 8 W, isotropic voxel

### Developing and optimizing HIPE resins for 3D printing



### 3D printing a complex structure - trabecular bone



**Scheme 1.** Optimization of porosity in inherently porous 3D-printed polyHIPE scaffolds and fabrication of hierarchically porous trabecular bone replicas from microCT images via 3D printing.

**Table 2.** EHA, IBOA, TMPTA, hypermer, beta-carotene, and tartrazine ratio (wt%).

Organic phase				Light absorber		
EHA (wt%)	IBOA (wt%)	TMPTA (wt%)	Hypermer (wt%)	Tartrazine <sup>a</sup> (wt%)		
39.70	39.70	15.90	4.70	0.02	0.04	0.08

<sup>a</sup> Tartrazine concentration with respect to the organic phase.

size: 39 micrometers [56, 57]. The standard reconstruction algorithm recommended by the manufacturer was used, using a polynomial correction to reduce beam hardening, based on a wedge phantom with insertions of  $1200 \text{ mg cm}^{-3}$  of hydroxyapatite (HA). A region of interest was inscribed inside the vertebral body excluding the endplates and the cortical shell, resulting in a parallelepiped of  $572 \times 572 \times 576$  voxels. The trabecular bone was segmented using a single level threshold equal to the value identified with the Otsu method increase of +5% [58] (ImageJ, National Institute of Health, United States). The trabecular bone microstructural parameters were calculated using 3D algorithms in CT Analyzer (V1.17.7.2, Bruker, MA, United States). Microstructural parameters included bone volume (BV), TV, BV fraction, (BV/TV), bone surface (BS), BS fractions (BS.BV and BS/TV), trabecular thickness (Tb.Th.), trabecular separation (Tb.Sp.), connectivity density (Conn.D) and degree of anisotropy (DA).

A surface (standard tessellation language, STL) file was created from the binary image (Amira 3D, Thermo Fisher Scientific, USA) simplifying the number of facets at approximately 1/10 of the nominal resolution, in order to reduce the size of the file, without losing the complexity of the trabecular structure. Conversion from DICOM image to printable image was performed in Amira 3D (Amira 3D 2022, Thermo Fisher Scientific, United States). A region of interest, of around  $22 \times 22 \times 22 \text{ mm}^3$ , was inscribed inside the volume of the vertebral body, excluding the cortical shell and the endplates. They grayscale image at 8 bit was segmented in order to identify what is bone (value on the image = 1) and not-bone (value on the image = 0). In particular, Otsu method with a correction of +5% (i.e. 72/255) was evaluated in ImageJ (Image J, National Institute of Health, United States) and applied as a single level segmentation threshold. A surface image was created from the segmented image through the module 'Generate Surface', using the border option to ensure the created surface was closed and deactivating any smoothing. Since the number of faces was too large to run other operations, a reduction of the number of faces was performed through a surface simplification employing an edge collapsing algorithm. In particular, the number of faces was reduced to 1/10 of the initial number (around 1.8 M faces). Finally, the file was exported to STL.

Autodesk Fusion 360 was used to add a base to the trabecular bone structure. Both designs were formatted as .stl files and then sliced using CHITUBOX Basic. The structures were 3D printed with a layer thickness of  $30 \mu\text{m}$ .

The 3D printing parameters, including exposure time, bottom layer count, and bottom exposure time, were presented in table 3. Careful optimization of the exposure time was conducted for each design to mitigate the risk of excessive curing. The overall duration

of the 3D printing process was approximately 10 min for the production of 30 disks with a diameter of 9 mm and a height of 1 mm. Similarly, it took approximately 20 min to print 30 disks with a diameter of 10 mm and a height of 2.5 mm. On the other hand, a batch consisting of 3 trabecular bone structures was 3D printed in approximately 6 h.

Upon completion of the 3D printing process, the 3D printed structures were washed with methanol to eliminate any residuals eluting from the polyHIPE, such as uncured resin. Subsequently, the structures were dried in an oven at  $65^\circ\text{C}$  for 24 h.

## 2.3. Characterization

### 2.3.1. Mercury intrusion porosimetry

The porosity of the polyHIPEs was measured using a mercury intrusion porosimeter (AutoPore V, Micrometrics). The contact angle of mercury and highest applied pressure were  $130^\circ$  and 60 000 psi (414 MPa), respectively.

### 2.3.2. Scanning electron microscope

The internal structure and outer surface of 3D-printed polyHIPE samples were imaged using a FEI Inspect F scanning electron microscope (SEM). To enhance the conductivity of the polyHIPEs, samples were gold-coated before imaging. An accelerating voltage of 5 kV was used for imaging. Pore diameters were measured using Image J software. For each sample, 50, 60, and 100 pores were measured to determine the average sizes of surface pores, internal pores, and interconnects, respectively ( $n = 3$ ). Moreover, a statistical correction factor of  $2/\sqrt{3}$  was applied to the measurements of internal pore size to compensate for the underestimation caused by uneven sectioning [59]. Also, the structure of 3D-printed trabecular bone samples was investigated by SEM.

### 2.3.3. Mechanical testing

To assess the mechanical properties of the polyHIPEs (10 mm diameter  $\times$  2.5 mm height disks), compression testing was conducted. A Mecmesin Multitest 2.5-dV mechanical testing machine was employed for this purpose. The compression was performed at a constant rate of  $1 \text{ mm min}^{-1}$ . The samples were loaded until they reached a displacement equal to 60% of the height of the sample being analyzed. The data were obtained using Vector Pro software. The stiffness was determined by analyzing the initial linear slope of the stress-strain plot, with a total of six replicates ( $n = 6$ ).

### 2.3.4. Cytocompatibility test

#### 2.3.4.1. Preparing samples for cell culture and cell seeding

The samples, in the form of disks measuring 9 mm in diameter and 1 mm in height, underwent a washing



**Table 3.** 3D printing parameters used to produce polyHIPE disks and trabecular bone.

Layer height ( $\mu\text{m}$ )	Bottom layer count	Exposure time (s)		Bottom exposure time (s)	Transition layer count	Bottom lift distance/Lifting distance (mm)
		Disk	Bone			
30	5	10	8	40	5	5
Bottom lift speed ( $\text{mm min}^{-1}$ )	Lifting speed ( $\text{mm min}^{-1}$ )	Bottom retract speed/Retract speed ( $\text{mm min}^{-1}$ )		Rest time before/after lift (s)	Rest time after retract (s)	
60	70	50		0	0.5	

process using methanol and PBS, followed by thorough drying. After that, the samples were sterilized with 70% ethanol (10 min, three times), followed by sterile PBS washes (10 min, three times). To improve cell attachment, the specimens (pure, 002 T, 004 T, 008 T and TCP) were pre-soaked in media overnight after sterilization. A human osteosarcoma cell line (MG-63 ATCC<sup>®</sup> CRL-1427<sup>TM</sup>) was used for this study. A cell culture medium containing 10% (v/v) FBS, 100 IU ml<sup>-1</sup> penicillin, 100 mg ml<sup>-1</sup> streptomycin, 2 mM L-glutamine, and 0.625 g ml<sup>-1</sup> amphotericin B at 37 °C and 5% CO<sub>2</sub> was used to maintain MG-63 cells in adherent cultures. MG-63 cells were cultured and allowed to grow in T75 flasks until they reached a confluency of 70%–80%. MG-63 cells were detached using trypsin and subsequently seeded at a density of  $3 \times 10^4$  cells per sample, with a volume of 20  $\mu\text{l}$ . Following the incubation at 37 °C and 5% CO<sub>2</sub> for 30 min, 1 ml of medium was added to the samples. The controls were TCP and pure. During the culture of the cells, the medium was changed every two days for 1, 4 and 7 days ( $N = 2$  and  $n = 3$ ).

#### 2.3.4.2. Cell metabolic activity

Cellular metabolic activity was assessed by measuring the reduction of resazurin, and cell viability was evaluated accordingly for pure, 002 T, 004 T, and 008 T disks ( $N = 2$  and  $n = 3$ ). The cells reduce the nonfluorescent, blue resazurin solution to a fluorescent, pink compound called resorufin, which can be detected using a fluorescent plate reader. In summary, a working solution of resazurin was prepared by diluting a 1 mM stock solution to a concentration of 100  $\mu\text{M}$  in a culture medium. The scaffolds were moved to a new well plate, and 1 ml of resazurin solution was added to each well. The plate was then incubated at 37 °C for 4 h. A spectrofluorometer (FLX800, BIO-TEK Instruments, Inc.) was utilized to measure the reduced solution from each scaffold. Triplicate samples of 200  $\mu\text{l}$  were measured, with excitation and emission wavelengths set at 540 nm and 630 nm, respectively. In each time interval, fresh scaffold/cell constructs were used for resazurin reduction assays.

#### 2.3.4.3. Immunofluorescence staining

On day 4, the samples labeled as pure, 002 T, 004 T, and 008 T were fixed with 3.7% formaldehyde (FA)

for 20 min. Afterwards, they were gently washed with PBS and submerged in 0.1% (v/v) Triton X 100 (in PBS) for 20 min. After washing the samples three times with PBS, a solution of phalloidin (FITC, Sigma Aldrich) was added to visualize F-actin filaments in the cells. The phalloidin solution was prepared by diluting 1:500 in PBS from the stock solution. The samples were then incubated for 30 min in the dark. After washing the samples three times with PBS, they were imaged using an LSM880 AiryScan Confocal Microscope (ZEISS, Germany) equipped with a 10 $\times$ /0.3 Plan-Neofluar objective. The FITC (green) channel was captured using 488 nm laser excitation and spectral detection ranging from 495 to 634 nm. Z-stack images (2580  $\times$  2580 pixels) were acquired for each sample and then projected into a single image.

#### 2.3.4.4. Alkaline phosphatase (ALP) activity

To investigate the ALP activity, seeded MG-63 cells on the disks (pure, 002 T, 004 T, and 008 T) were cultured for 28 days ( $N = 2$  and  $n = 3$ ). ALP is a common marker of osteogenesis, used as an initial marker of osteoblast differentiation. An increase in the level of ALP suggests active bone formation may be occurring. The 28-day culture period was selected so that MG-63 cells could progress through different stages of differentiation and reach a more advanced osteoblast-like phenotype.

##### 2.3.4.4.1. Cell digestion

Cell digestion was carried out to produce lysates for dsDNA quantification and ALP activity assays. Cell culture media was removed and samples were washed twice in 1X PBS. 500  $\mu\text{l}$  of cell digestion buffer (CDB) (10 vol% CAB (1.5 M Tris-HCL, 1 mM ZnCl<sub>2</sub>, 1 mM MgCl<sub>2</sub> in diH<sub>2</sub>O) in diH<sub>2</sub>O with 1 vol% Triton-X100) was added to the well and incubated at RT for 30 min. Wells were then scraped, and the CDB (and scaffolds when in 3D culture) were transferred to 1.5 ml Eppendorf tubes and refrigerated for 12 h. After refrigeration, lysates underwent a freeze-thaw cycle (–80 °C for 10 min, 37 °C for 15 min) three times, vortexing at the end of each cycle. Samples were then centrifuged at 10 000 rpm for 5 min.

#### 2.3.4.4.2. Total dsDNA assay

Total dsDNA was measured using a fluorescent Quant-iT dsDNA high-sensitivity assay kit (Invitrogen, UK). The Quant-iT dsDNA Assay reagent was diluted 1:200 in the Quant-iT DNA Assay Buffer. 90  $\mu\text{l}$  of this working solution was added in triplicate to a black 96-well plate, with 10  $\mu\text{l}$  of cell lysate, then added to each well. The 96-well plate was placed in a microplate reader (Tecan infinite 200-pro) and was gently shaken for 10 s to fully mix lysate and reagent and left for a further 10 min to allow for conjugation of dsDNA and assay reagent. The plate was read at excitation 485 nm and emission 52 nm.

#### 2.3.4.4.3. ALP assay

To quantify ALP activity, a Pierce™ pNPP Substrate Kit (Thermo Scientific) was used according to the manufacturer's instructions. 5 mg para-nitrophenyl phosphate (pNPP) was dissolved per 5 ml of 20 vol% diethanolamine buffer in  $\text{dH}_2\text{O}$  to form the assay substrate. To a 96 well-plate. 180  $\mu\text{l}$  of ALP substrate was added to a 96-well plate, with 20  $\mu\text{l}$  of cell lysate added in triplicate, and incubated at room temperature for 30 min. The absorbance of each well was measured at 405 nm every min for a further 30 min in a microplate reader set at 25 °C (Tecan Infinite 200-pro). Activity is expressed as nmol pNPP per minute per dsDNA (nmol pNPP/min/dsDNA), where one absorbance value equals 19.75 nmol of pNPP. dsDNA was quantified and ALP activity was normalized to this, to account for differences in cell populations observed from resazurin reduction assays and fluorescent imaging.

#### 2.3.4.5. Cell adhesion and morphology

To examine the cell morphology on the pure, 002 T, 004 T, and 008 T samples, MG-63 cells ( $3 \times 10^4$  cells) were seeded onto the surfaces. The seeded specimens were then incubated at 37 °C and 5%  $\text{CO}_2$  for 4 days. Subsequently, the samples were washed and fixed with PBS and 3.7% FA, respectively. Dehydration was carried out using a series of ethanol solutions (30%, 50%, 70%, 90%, and 100% ( $\times 2$ )). Finally, the dried samples were sputter-coated with gold and observed using SEM. False-colored SEM images were made using Adobe Photoshop CS6 (by changing the color balance, creating a duplicate layer, clipping the mask, and changing hue/saturation).

#### 2.3.4.6. Cell seeding and observing on 3D-printed trabecular bone samples

##### 2.3.4.6.1. Cell seeding on 3D-printed trabecular bone samples

The 3D-printed samples, designed as trabecular bone with dimensions of 10 mm width, 10 mm length, and 10 mm height, were subjected to a washing process using methanol and PBS and then thoroughly dried.

The sterilization, cell culture, and cell seeding process for the trabecular samples were similar to the disk samples, with the exception of the number of MG-63 cells used for seeding, which was  $10 \times 10^4$  cells per sample (150  $\mu\text{l}$ ). Due to the larger size of these samples compared to disks, the cell seeding was carried out in two steps. Initially, half of the cells (75  $\mu\text{l}$ ) were seeded on top of the specimen and incubated for 30 min. Subsequently, the sample was flipped over, and the remaining cells (75  $\mu\text{l}$ ) were seeded, followed by another 30 min incubation period. Finally, the media was added to the samples (figure S6) ( $N = 3$  and  $n = 3$ ).

##### 2.3.4.6.2. DAPI/FITC staining and confocal imaging of 3D-printed trabecular bone samples

In order to visualize the MG-63 cells that were seeded onto the 3D-printed trabecular bone samples and to study cell migration within these structures, DAPI and FITC staining was conducted on specimens on both day 14 and day 28. The specimens were divided into three sections, and the central/middle segment was selected for confocal imaging.

On days 14 and 28, samples were fixed with 3.7% FA for a duration of 30 min. Subsequently, they were delicately rinsed with PBS and immersed in a 0.1% (v/v) solution of Triton X 100 in PBS for 20 min. Following three washes with PBS, a phalloidin solution (FITC, Sigma Aldrich, by diluting 1:500 in PBS from the stock solution) was added to visualize the F-actin filaments within the cells. Incubation was conducted in the dark for 30 min after that. After three washes of PBS, the cell nuclei were stained with a 4',6-diamidino-2-phenylindole (DAPI, Sigma Aldrich, by diluting 1:1000 in PBS from the stock solution), followed by a 15-minute incubation in darkness. Samples were washed three times with PBS, and then they were imaged using a Nikon CSU-W1 Spinning Disk Confocal equipped with a 10x Plan Apo  $\lambda$  objective with a disk position of 25  $\mu\text{m}$ . A 405 nm excitation laser was employed to stimulate the DAPI (blue) images, and their spectral detection was conducted within the 410–495 nm range. A 488 nm excitation laser was used to capture FITC (green) images and spectral detection ranging from 495 to 634 nm. Bit depth (bits per pixel) of 12-bit was used, and Z-stack images (1412  $\times$  1412 pixels) with a step of 2.5  $\mu\text{m}$  were acquired for each sample. Images were created by NIS-Elements AR 5.42.03.

##### 2.3.4.6.3. Cell adhesion and morphology on the 3D-printed trabecular bone structure

To investigate the cell morphology on the 3D-printed trabecular bone sample, some specimens with similar conditions to DAPI/FITC imaging were used to analyze cell adhesion and morphology of MG-63 cells after 14 and 28 days. The preparation of samples for SEM imaging was the same as 2.2.3.4.5. section.

#### 2.3.4.6.4. Micro computed tomography of 3D-printed trabecular bone structures

3D-printed trabecular bone structures were cut into small cubic samples (1 cm × 1 cm × 1 cm) and four specimens were micro CT imaged (Skyscan1172, Bruker) in order to visualize the 3D-printed trabecular bone structure, by using the following scanning parameters: current: 149  $\mu$ A, voltage: 40 kVp, exposure time: 295 ms, power:  $\sim$ 6 W, rotation step 0.7 deg, 180 deg rotation, isotropic voxel size 7.49  $\mu$ m [57]. The reconstruction of the images was performed with the micro CT manufacturer software (NRecon, version 1.6.9.4, Bruker) using Ring artifact correction equal to 10.

Each of the grey level images was then segmented to identify the scaffold's structure, de-noised with a despeckling algorithm, and 3D rendered (figure 7).

#### 2.3.5. Statistical Analysis

All statistical analysis was undertaken in Origin Pro 2023. One-way ANOVA with Tukey's multiple comparison analysis was applied to assess significant differences. Differences were considered significant when  $p < 0.005$ . The number of replicates utilized in the study is specified in both the Materials and Methods section as well as the figure legend.

### 3. Results and discussion

Previous literature has demonstrated that light absorbers enable the production of polyHIPE or polyMIPE porous scaffolds with open surface porosity [13, 36]. Additionally, it affects the degree of porosity and pore sizes of the final product [36]. If these porous scaffolds are intended for use for producing physiological replicas of trabecular bone, understanding the overall impact of the light absorbers on the porous structure is significant, in particular the surface porosity, which is essential for cell ingrowth into the scaffold. In this study we explored the production of an inherently porous resin to print anatomical mimics of human trabecular bone and explore cell proliferation on these multiscale porous scaffolds.

#### 3.1. The effect of tartrazine as a light absorber on the porous structure

In this study, polyMIPEs were fabricated in 4 different formulations, which included samples without tartrazine and others with different concentrations of tartrazine at 0.02 wt%, 0.04 wt%, and 0.08 wt%. To simplify the categorization, these groups were denoted as pure, 002 T, 004 T, and 008 T, respectively.

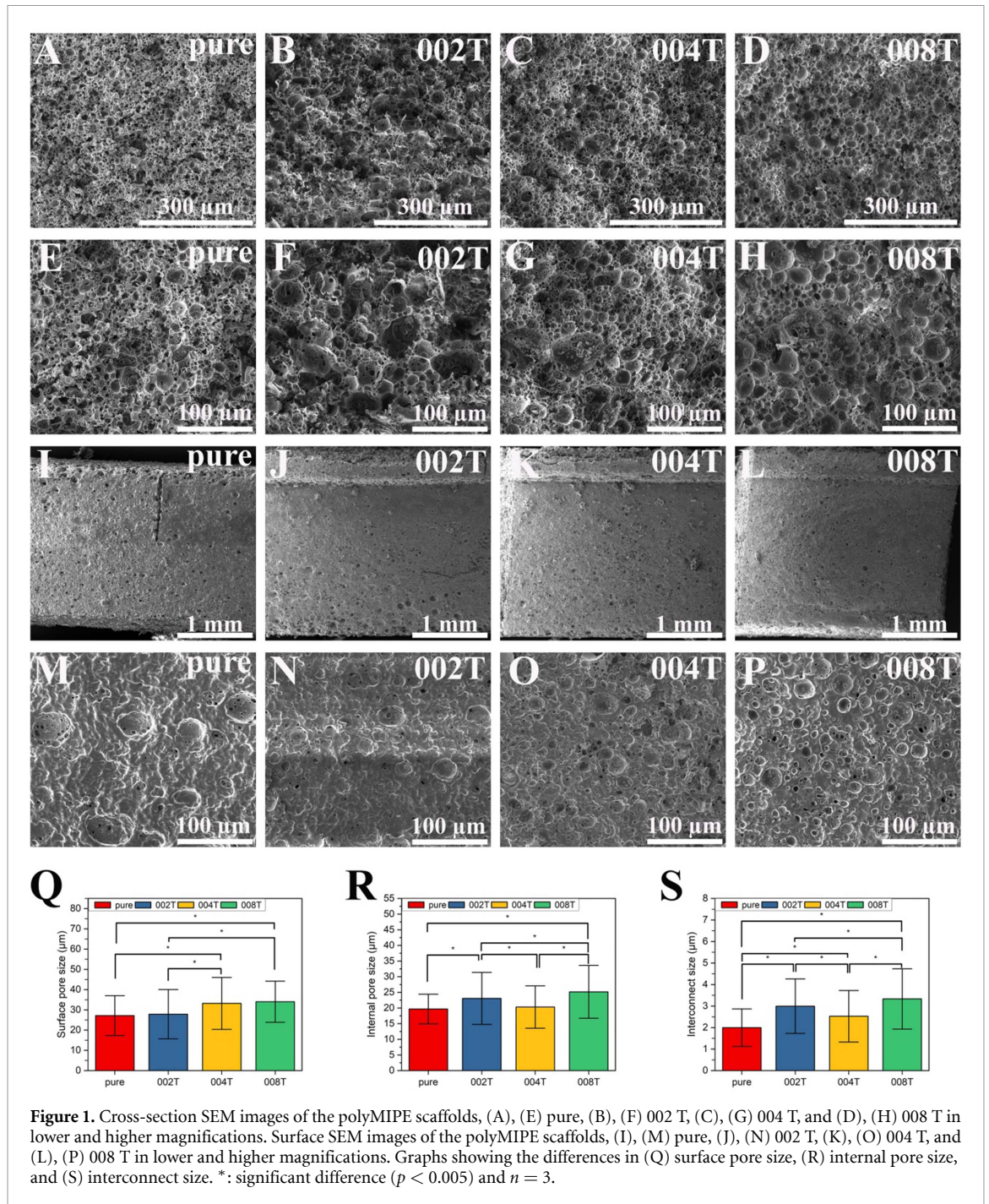
The representative scanning electron microscope (SEM) images are provided in figures 1 and 2. In figure 1, SEM images captured from the cross-section and the surface of the samples are shown at lower magnifications and at higher magnifications. The cross-section SEM images were used to measure

internal pore sizes and interconnect sizes, whereas surface SEM images were used to measure surface pore sizes.

The surface pore sizes, internal pore sizes, and interconnect sizes of the samples are presented in table 4. The statistical differences among them are demonstrated in figures 1(Q), (R) and S, respectively. The surface pore sizes varied from  $27.18 \pm 9.81 \mu\text{m}$  to  $34.02 \pm 10.15 \mu\text{m}$ , increasing with the tartrazine ratio. There were significant differences among most categories except between pure-002 T and between 004 T–008 T categories. In contrast, the internal pore sizes did not exhibit a clear correlation. However, all categories were statistically different from each other, except for the pure-004 T category. The internal pore sizes for the pure, 002 T, 004 T, and 008 T categories were measured as  $19.67 \pm 4.74$ ,  $23.07 \pm 8.32$ ,  $20.32 \pm 6.77$ , and  $25.17 \pm 8.46 \mu\text{m}$ , respectively. Similarly, the interconnect sizes ranged between  $1.99 \pm 0.87$  and  $3.33 \pm 1.40 \mu\text{m}$  without displaying any specific trend. The pure category had the smallest interconnect size, while the 008 T category had the largest. Additionally, all categories showed statistically significant differences in terms of interconnect sizes. The surface pore sizes, internal pore sizes, and interconnect sizes hold significance in bone tissue engineering applications, as the porous structure is considered one of the main criteria [60–62]. Notably, the following sample categories exhibited significant differences across all three comparisons: pure-008 T, 002 T–004 T, and 002 T–008 T.

The pore size distributions, plotted against relative frequency (%), and their Gaussian fits are presented in the supporting information (figures S1–S3). According to these analyses, all histograms showed that the samples predominantly consisted of smaller pores, with fewer larger pores present whereas pure samples showed a near-symmetric distribution. In all categories, 002 T, 004 T, and 008 T exhibited increasing right-skewness, with the largest skewness observed in 008 T.

Furthermore, figure 2 demonstrates the top layer, representing the last cured layer and the bottom layer, representing the initial cured layer of the polyMIPE disks. In addition, the graphs showing the statistical differences among the categories are presented in figures 2(I) and (J). The pore sizes for the Pure, 002 T, 004 T, and 008 T categories measured from the top layer were  $29.85 \pm 8.98$ ,  $33.92 \pm 11.01$ ,  $31.07 \pm 10.35$ , and  $29.02 \pm 8.41 \mu\text{m}$ , respectively, while the pore sizes measured from the bottom layer were  $72.87 \pm 19.18$ ,  $69.44 \pm 17.80$ ,  $76.80 \pm 28.65$ , and  $76.14 \pm 28.56 \mu\text{m}$ , respectively. Although there were no significant differences among the categories in the bottom pore sizes, the Pure-002 T and 002 T–008 T categories showed statistically significant differences in the top pore sizes. Moreover, their pore size distributions are presented in figures S4 and S5.



All samples exhibited right-skewness, indicating a higher frequency of smaller pores, but the bottom layer showed a broader range of larger pores compared to the top layer.

Based on the measured pore sizes, it is clear that pore sizes decrease during 3D printing when comparing the top layer, bottom layer, and internal pore sizes. The reason for this is that the printing layer thickness limits the formation of larger pores.

The degree of porosity in the pure samples was measured at 63.92%. In contrast, the samples containing tartrazine exhibited a lower porosity, approximately around 56%. This result indicated a significant decrease in porosity upon the addition of

tartrazine. Furthermore, as the amount of tartrazine increased, no significant further decrease in porosity was observed. While tartrazine creates a more open surface with larger pores, it causes a decrease in overall porosity due to its potential to reduce emulsion stability, combined with the up-and-down movement of the 3D printing platform [36]. The print platform moves up and down to separate each printed layer from the resin tank, then returns to a thickness of 30  $\mu\text{m}$  (printing layer thickness) for the next photopolymerization cycle. This complex sequence for each layer could significantly impact emulsion stability and overall porosity, as evidenced by the difference between the porosities of the prepared HIPE

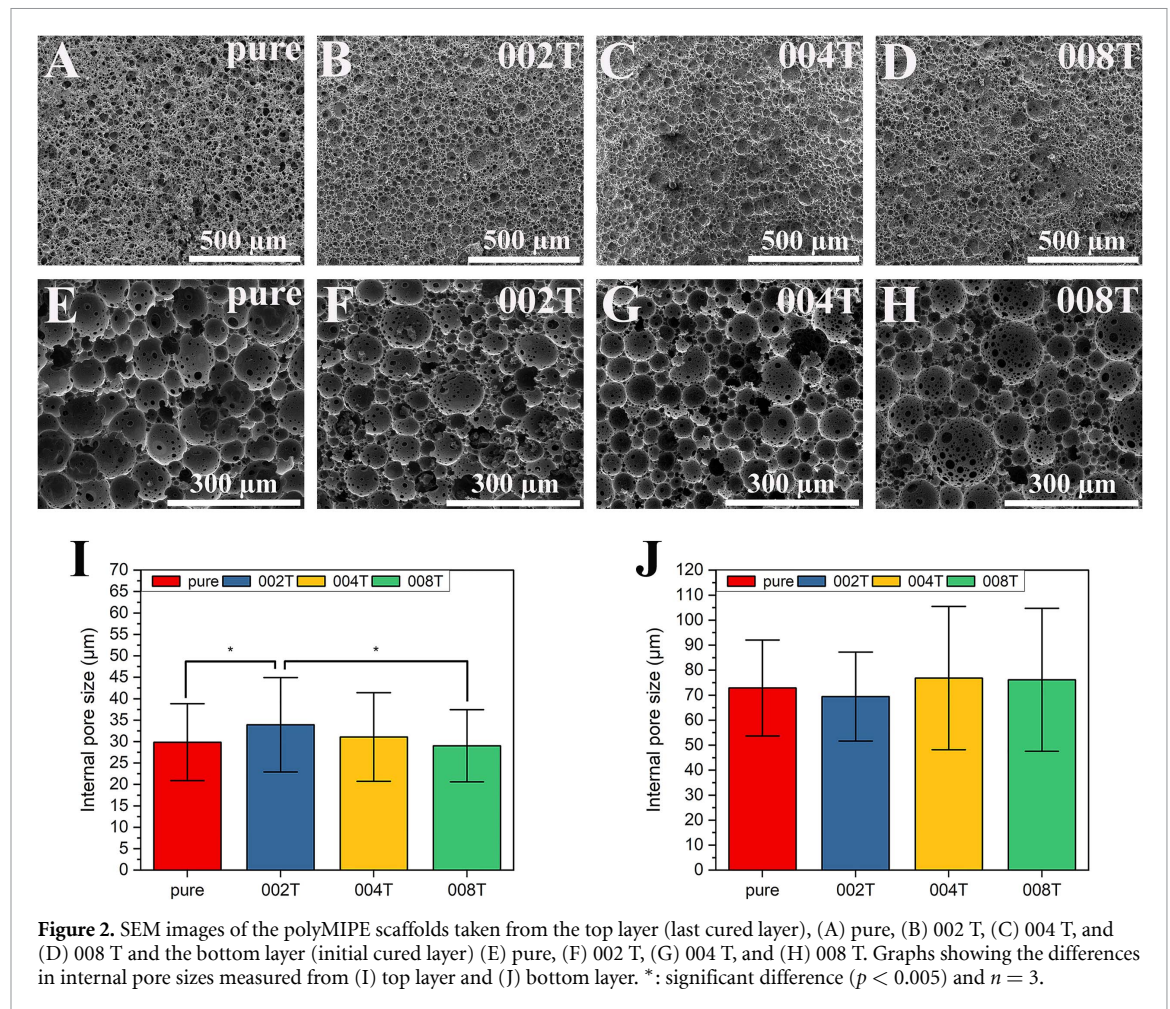


**Figure 2.** SEM images of the polyMIPE scaffolds taken from the top layer (last cured layer), (A) pure, (B) 002 T, (C) 004 T, and (D) 008 T and the bottom layer (initial cured layer) (E) pure, (F) 002 T, (G) 004 T, and (H) 008 T. Graphs showing the differences in internal pore sizes measured from (I) top layer and (J) bottom layer. \*: significant difference ( $p < 0.005$ ) and  $n = 3$ .

**Table 4.** Surface pore size ( $\mu\text{m}$ ), internal pore size ( $\mu\text{m}$ ), interconnect size ( $\mu\text{m}$ ), porosity (%), stiffness (MPa) values of polyMIPE scaffolds.

Samples	Surface pore size ( $\mu\text{m}$ )	Internal pore size ( $\mu\text{m}$ )	Interconnect size ( $\mu\text{m}$ )	Porosity (%)	Stiffness (MPa)
Pure	$27.18 \pm 9.81$	$19.67 \pm 4.74$	$1.99 \pm 0.87$	63.92	$1.10 \pm 0.36$
002 T	$27.87 \pm 12.16$	$23.07 \pm 8.32$	$2.99 \pm 1.27$	57.20	$0.74 \pm 0.25$
004 T	$33.18 \pm 12.84$	$20.32 \pm 6.77$	$2.53 \pm 1.20$	55.64	$0.75 \pm 0.28$
008 T	$34.02 \pm 10.15$	$25.17 \pm 8.46$	$3.33 \pm 1.40$	55.70	$1.03 \pm 0.34$

(80% internal phase) and the 3D-printed pure polyHIPE (63.92%), a reduction of more than 15%. Since the addition of tartrazine caused an additional  $\sim 8\%$  reduction, it is likely that it further compromised stability during 3D printing.

In addition to these, their mechanical properties were similar to each other with no statistical difference. The stiffness of all 4 categories was between  $0.74 \pm 0.25$  and  $1.10 \pm 0.36$  MPa. The incorporation of tartrazine did not affect the stiffness in both negative and positive way.

### 3.2. Cell metabolic activity

The *in vitro* cell metabolic assays were conducted on pure, 002 T, 004 T, and 008 T samples using resazurin dye and human osteosarcoma (MG-63) cell lines for a duration of up to 7 days. Cells cultured on pure,

002 T, 004 T, and 008 T showed no evidence of a decrease in metabolic activity (figure 3(A)), indicating that the samples were not cytotoxic. Among the samples, 008 T exhibited the highest values of relative fluorescence (RF) on day 4 and 7. Compared to day 1 ( $2965.56 \pm 515.47$ ) the RF of 008 T tripled on day 4 and was 5 times higher on day 7 ( $16578.33 \pm 378.36$ ) indicating high cell proliferation on these scaffolds. As shown in figure 3(A), RF values display an upward trend from 002 T to 004 T and continue increasing to 008 T, consistently across all time points. This trend, which can be attributed to the increase in surface pore sizes, is reflected in the increasing right-skewness of surface pore size distributions observed across all categories—002 T, 004 T, and 008 T—with the largest skewness noted in 008 T (figure S1). The size of pores in the scaffold can have an impact on cell

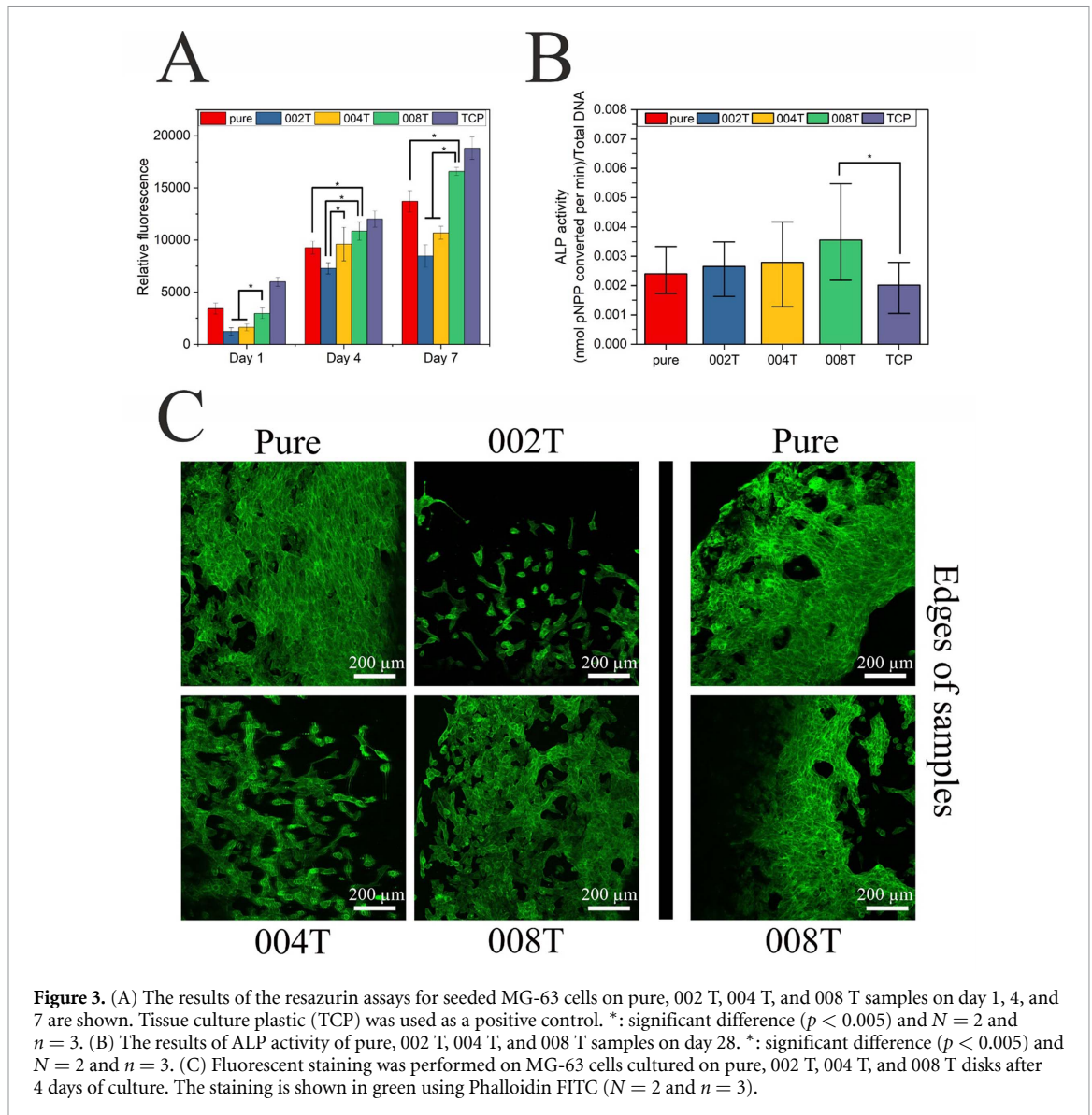


**Figure 3.** (A) The results of the resazurin assays for seeded MG-63 cells on pure, 002 T, 004 T, and 008 T samples on day 1, 4, and 7 are shown. Tissue culture plastic (TCP) was used as a positive control. \*: significant difference ( $p < 0.005$ ) and  $N = 2$  and  $n = 3$ . (B) The results of ALP activity of pure, 002 T, 004 T, and 008 T samples on day 28. \*: significant difference ( $p < 0.005$ ) and  $N = 2$  and  $n = 3$ . (C) Fluorescent staining was performed on MG-63 cells cultured on pure, 002 T, 004 T, and 008 T disks after 4 days of culture. The staining is shown in green using Phalloidin FITC ( $N = 2$  and  $n = 3$ ).

attachment and spread [63, 64]. On day 1, the metabolic activity of the pure and 008 T samples was similar, but starting on day 4, the activity showed a significant increase. Adequate cell attachment is essential for maintaining cell viability and promoting metabolic activity [63, 65]. Osteoblasts have a preference for larger pores, as it aids cell ingrowth and mineralization of the scaffold [66, 67]. Furthermore, the pure sample exhibited a good range of cell metabolic activity, which can be attributed to the highly porous structure facilitated by EHA-IBOA polyMIPEs. Previous studies in our group have demonstrated that EHA-IBOA polyHIPeS effectively support MG-63 cells by promoting cell attachment, growth, and proliferation [2].

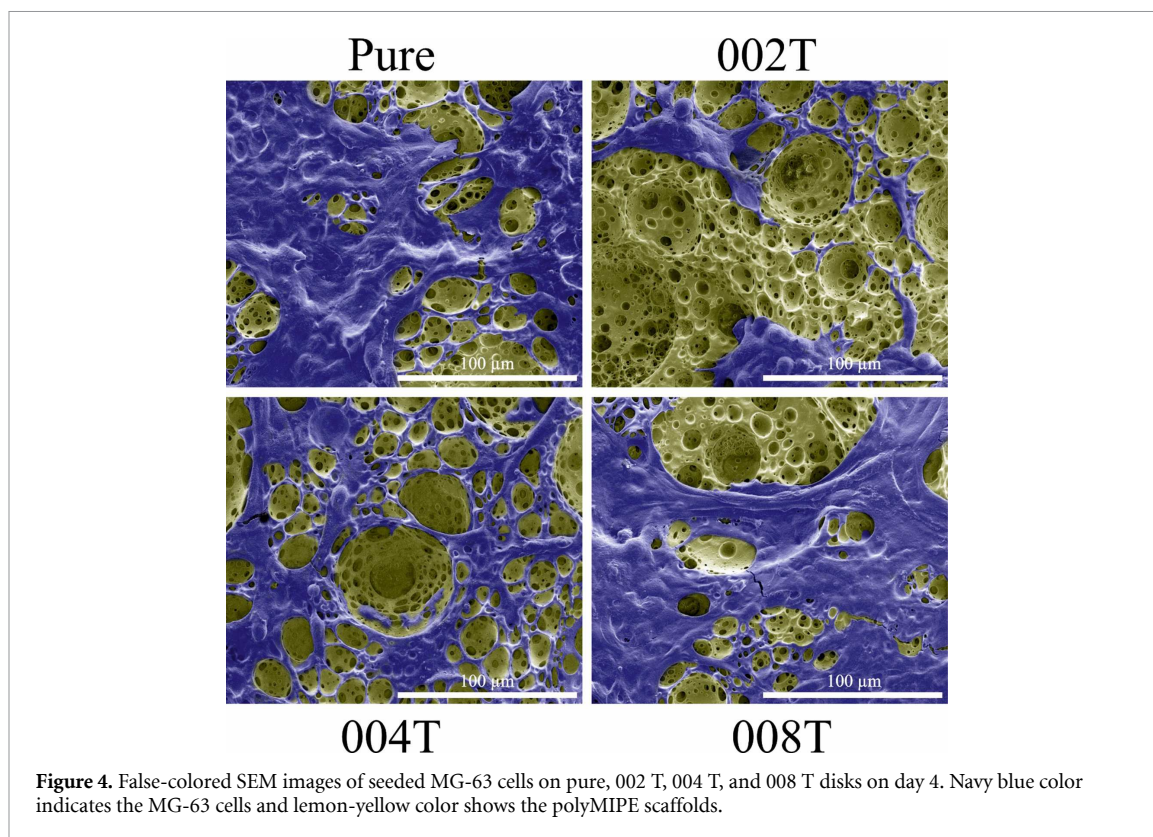
### 3.3. Immunofluorescence staining

After 4 days of culture, MG-63 cells were observed on pure, 002 T, 004 T, and 008 T disks using an LSM880 AiryScan Confocal Microscope (ZEISS, Germany). The cells were stained with FITC-Phalloidin for

visualization (staining F-actin) (figure 3(C)). Figure 3(C) indicates a higher presence of MG-63 cells on pure and 008 T samples, consistent with the resazurin results obtained. MG-63 cells on pure and 008 T samples exhibited a tendency to form a confluent monolayer, whereas on 002 T and 004 T samples, the cells were less confluent, and their morphology appeared epithelial-like, with some cells exhibiting rounded shapes and others polygonal shapes [68, 69]. At the initial time points, the pure and 008 T samples showed similar cell attachment and metabolic activity, which may be attributed in part to their comparable stiffness (table 4 –  $1.10 \pm 0.36$  MPa for pure and  $1.03 \pm 0.34$  MPa for 008 T), a property known to influence cell behavior.

### 3.4. ALP activity

After 28 days of culture, 008 T showed significantly higher ALP compared to that of the TCP control (figure 3(B)). As previously mentioned, 008 T scaffolds had an increased pore size. Larger pore size



leads to a higher surface area, facilitating greater cell attachment and spreading. This enables more efficient cell-matrix interactions and promotes cell adhesion and proliferation. Additionally, it may enhance the osteogenic activity of MG-63 cells, potentially attributed to the increased ALP activity. The exact range scale of porosity for optimal bone tissue formation is often described in multiple length scales, the nanoporous and microporous scale, which is needed for cell infiltration, and a macroporous scale, which may span from a few 100 microns to millimetres, to allow for efficient nutrient transfer, blood infiltration and osseointegration in the case of implanted scaffolds [70]. On the micrometer scale porosity, various researchers have described varying optimal porosities, depending on cell type and scaffold material. Kuboki *et al* showed that larger pore interconnects further benefited bone formation due to an increase in nutrient diffusion and providing a high level of oxygenation to infiltrated cells [71]. In the present study, 008 T was shown to have the largest interconnects between pores, which may also play a role in the increased cellular proliferation and ALP activity.

### 3.5. Cell adhesion and morphology

Scanning electron microscopy (SEM) was used to observe MG-63 cell morphology on pure, 002 T, 004 T, and 008 T scaffolds with high-resolution, detailed images of the cell surface, revealing the 3D cell structure and surface features. Figure 4 illustrates the elongation and spreading of MG-63 cells on all samples [72], including pure, 002 T, 004 T,

and 008 T, over the pores of the polyMIPE scaffolds on day 4. False-colored SEM images (figure 4) aid observation of the MG-63 cells on the samples more clearly (non-false-colored SEM images are provided in figure S7). Figure 4 shows that MG63 cells adhered to all specimens, with greater confluence and spreading observed on the pure and 008 T samples. More adhered and proliferated cells were observed on the surface of 008 T compared to 004 T and 002 T. However, consistent with the resazurin and immunofluorescence staining results, there was a trend among these samples: 008 T > 004 T > 002 T, indicating a higher cell presence and clustering on 008 T. As previously mentioned, this trend may be attributed to the changes in surface porosity caused by the inclusion of tartrazine. Higher concentrations of tartrazine led to larger surface pore sizes, which could explain the observed differences in cell adhesion and proliferation among the samples.

Given the results obtained, 008 T provided greater support for MG-63 cells than the other groups. Hence, this particular sample was selected for the 3D printing of the trabecular bone structure and subsequent investigations.

### 3.6. Inherently porous 3D-printed trabecular bone structure

We used an anatomically correct, patient derived model of trabecular bone, and we have been able to reproduce this model with the inherently porous printing resin with a resolution of  $\sim 150 \mu\text{m}$ , in accordance with our previous studies [36, 38]. Based

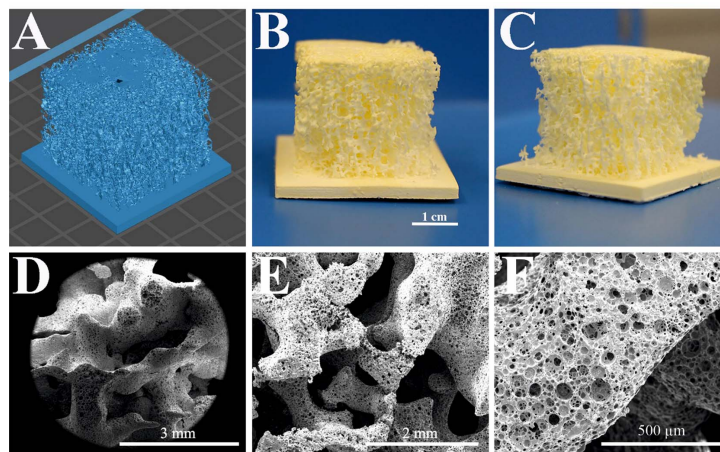


**Figure 5.** (A) 3D design of the trabecular bone structure, (B and C) 3D printed trabecular bone structure from different perspectives. (D, E and F) SEM images of the 3D-printed trabecular bone structure with various magnifications.

on our previous studies, we successfully reproduced 5 mm × 5 mm cylinders with an aspect ratio of  $0.97 \pm 0.03$  and a regular lattice structure with a strut thickness of  $0.29 \pm 0.08$  mm. The small standard deviations demonstrate that the structures are reproducible from the emulsion-based resin via 3D printing. The 3D design of the trabecular bone structure utilized in this study, along with digital images showcasing the 3D printed trabecular bone structures from various perspectives, are illustrated in figure 5. The spongy structure of the trabecular bone was fabricated to closely resemble the original design file, as depicted in figures 5(A)–(C). Also, SEM images show the structure of trabecular bone containing micro and macropores (figures 5(D)–(F)).

### 3.6.1. DAPI/FITC staining and confocal imaging of 3D-printed trabecular bone structures

For the 3D printing of trabecular bone structures, the HIPE resin chosen was 008 T. Employing HIPEs as a resin/ink for 3D printing scaffolds for bone tissue engineering offers essential features for this application, such as the presence of both microporous ( $<5 \mu\text{m}$  pores) and macroporous ( $>100 \mu\text{m}$  pores) structures [68, 73]. Larger pores are conducive to direct osteogenesis, as they facilitate vascularization and provide better nutrient transfer and oxygenation. On the other hand, smaller pores lead to osteochondral ossification, although the specific type of bone ingrowth is influenced by both the material properties and the pore geometry [68, 74, 75]. Cell adhesion, proliferation, and colonization of the 3D-printed trabecular bone scaffold are shown in figure 6, A to D, after 14 and 28 days of cell culture. This demonstrates that all scaffolds offer a favorable 3D substrate for MG-63 attachment. Moreover, the interconnected channels enable cell migration from the initial seeding position at the top of the scaffold to the lower regions. As can be seen in figures 6(A)–(D), after 28 days of cell culture, a noticeable increase in cell proliferation

and migration compared to day 14 was observed. The presented outcomes indicate the potential of 008 T HIPE resin for bone tissue engineering applications. Furthermore, it demonstrates suitability for 3D printing complex structures, including the successful fabrication of trabecular bone models that effectively support cell growth, proliferation, and migration. These findings align with previous research in similar [15, 76]. Creating intricate structures such as trabecular bone using suitable resins for bone tissue engineering holds significant potential. For example, this approach could eventually lead to enhanced personalized fracture risk assessments through procedures like CT scanning, 3D printing, and mechanical testing of patient-specific bone replicas for those afflicted by severe bone resorption [77, 78]. Incorporation of these *in vitro* 3D tissue mimics in microphysiological systems, with inclusion of a vascular component (as recently highlighted by Chesnais *et al* [79]), could provide next generation models of healthy and diseased bone. Another potential application is the replication of these 3D-printed scaffolds in biodegradable materials to replace a substantial section of the vertebra in cases of peripheral lesions, or trabecular bone in critical bone defects. Although the construct's stiffness remains lower in comparison to bone, its structural compatibility holds the potential to enhance bone cell attachment, and subsequently, osteointegration.

### 3.6.2. Cell adhesion and morphology on the 3D-printed trabecular bone structure

The false-colored SEM images are given in figures 6(E)–(H) for day 14 and figures 6(I)–(L) for day 28 for better visualization of the MG-63 cells (non-false-colored SEM images are provided in figure S8). SEM images were taken from different parts of the samples (specimens were cut, and middle sections were investigated); images show that MG-63 cells were elongated, spread and well-flattened after day 14



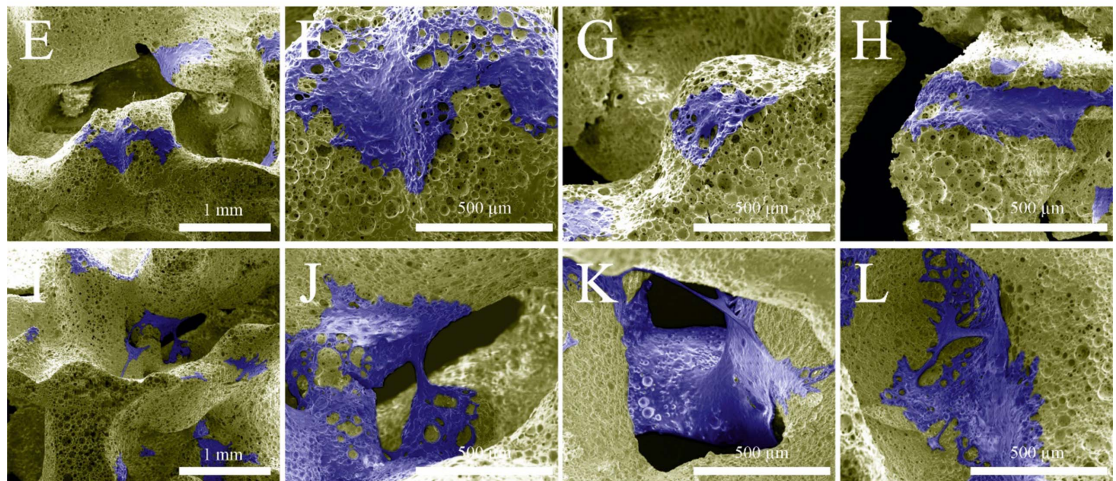
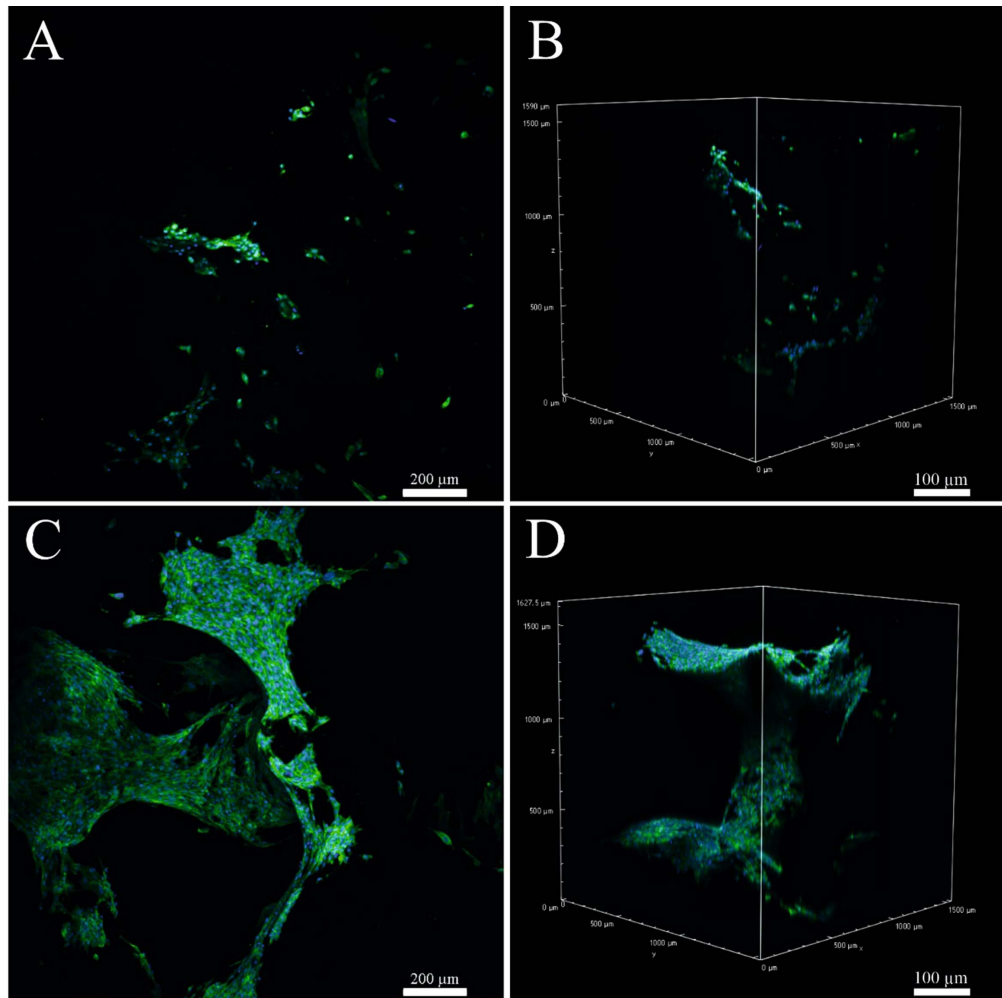


**Figure 6.** Confocal images of seeded MG-63 cells on 3D-printed trabecular bone samples after being cultured for 14 and 28 days (Blue: DAPI and green: Phalloidin FITC). (A) and (C) Max intensity projection of z-stack images on day 14 and day 28, respectively. (B) and (D) 3D volume view of z-stack images from  $YZ = 45^\circ$  view plane on day 14 and day 28, respectively. False-colored SEM images of seeded MG-63 cells on the 3D-printed trabecular structures on day 14 (E) to (H) and day 28 (I)–(L). Navy blue color indicates the MG-63 cells, and lemon-yellow color shows the polyMIPE scaffolds.

and day 28. Further, the SEM study, on both day 14 and day 28, confirmed the infiltration and migration of MG-63 cells deep into the 3D porous network of the trabecular structures, in agreement with confocal

results. SEM images of day 28 showed a greater extent of the MG-63 cell ingrowth, which resulted in helping the formation of the bridges across the pores [80–82].

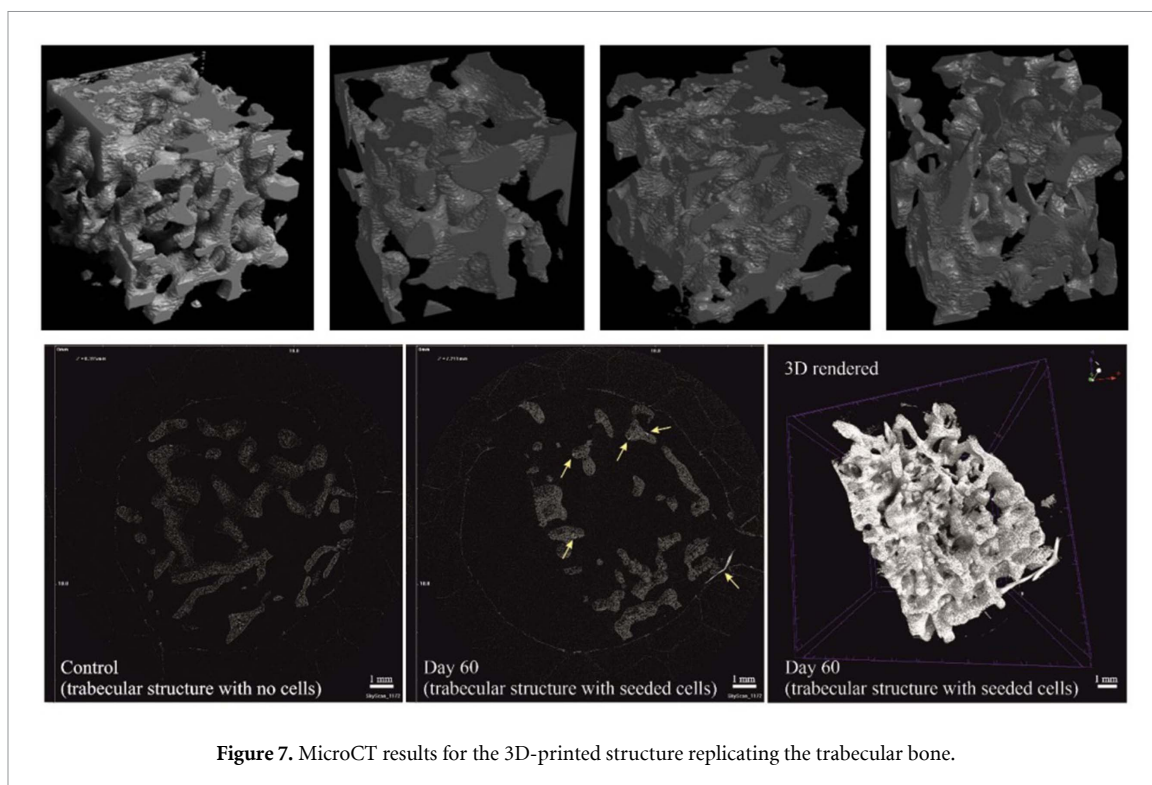


Figure 7. MicroCT results for the 3D-printed structure replicating the trabecular bone.

Table 5. Standard equivalent bone morphometric parameters for the 3D-printed structure replicating the trabecular bone.

BV/TV (%)	BS/BV (1 mm)	BS/TV (1 mm)	Tb.Th.(mm)	Tb.Sp.(mm)	Conn.D. (1 mm)	DA (.)
$28.28 \pm 4.63$	$18.63 \pm 3.89$	$5.23 \pm 1.21$	$0.37 \pm 0.07$	$0.90 \pm 0.19$	$8.79 \pm 3.94$	$0.84 \pm 0.04$

### 3.6.3. Micro computed tomography imaging of 3D-printed trabecular bone structures

3D-printed trabecular bone structures after 60 days of cell growth were also investigated via micro CT imaging (figure 7). 3D morphometric assessment of the 3D-printed microstructure was performed (CTAn, Bruker). Standard equivalent bone morphometric parameters as the TV, Segmented BV, BV fraction (BV/TV), BS ratio (BS/BV), BS density (BS/TV), Tb.Th., Tb.Sp., Conn.D. and DA are reported in table 5.

As expected, most of the morphometric parameters calculated for the 3D-printed structure are within the range of values found for the trabecular bone in the human radiologically healthy or metastatic vertebrae [57, 58, 83]. Nevertheless, the density and thickness or the trabeculae-like structures in the 3D-printed model ( $\sim 28\%$ ,  $\sim 370$  micrometers) were higher than the average properties of the trabecular bone cube used to generate the input sub-images for the 3D printed specimens ( $\sim 8\%$ ,  $\sim 170$  micrometers) and the typical trabecular BV fraction and thickness reported for healthy human vertebral trabecular bone ( $\sim 13\%$ ,  $\sim 150$  micrometers) [84] and radiologically

healthy (range: 7.4%–14.5%, range: 154–177 micrometers) or metastatic (range: 8.4%–72.6%, range: 155–398 micrometers) human vertebral bodies [58]. This is probably due to two reasons: (1) the 3D-printed structure was based on a micro CT image of a radiographically healthy vertebra (from clinical CT analyses) from a subject who suffered of bone metastases and therefore was treated with bisphosphonates, which increases the bone density; (2) possible differences in microstructural properties between the large trabecular bone cube and the smaller cubes cut from it and used for micro CT imaging could also be due to the intrinsic heterogeneity of the trabecular structure within the cube; (3) the highest resolution that can be printed using HIPes is  $150 \mu\text{m}$ , however when thinner struts are too close to each other, they might merge during printing, causing thicker struts. Nevertheless, the approach used in this study enabled the creation of 3D-printed structure with a complexity similar to human trabecular bone and microstructural properties similar to human femoral trabecular bone (thicker and denser than human vertebral trabecular bone; range of BV/TV:  $\sim 20\%$ – $40\%$ ; range of Tb.Th 230–350 micrometers [85],

highlighting its potential for developing scaffolds for bone replacement.

#### 4. Conclusions

In conclusion, this study explored how tartrazine, as a light absorber, impacts acrylate-based polyMIPES fabricated via vat photopolymerization. We examined how varying concentrations of tartrazine affected the porosity of 3D-printed polyMIPES disks and evaluated the behavior of MG-63 cells on these structures. Tartrazine proved to be an effective tool for controlling scaffold porosity, which is crucial for tailoring scaffold properties to meet specific tissue engineering requirements. Furthermore, the successful 3D printing of an inherently porous trabecular bone structure highlights the potential of this method for creating bone models and applications such as bone-on-chip.

The cytocompatibility of 3D-printed polyMIPES disks with different concentrations of tartrazine was tested using MG-63 cells. Resazurin assays showed that cells exhibited no decrease in metabolic activity over 7 days. Notably, the samples with 0.08 wt% tartrazine (008 T) showed the highest levels of cell metabolic and ALP activity, likely due to their larger pores. Immunofluorescence staining demonstrated excellent cell attachment and spreading, especially on the 008 T samples. Scanning electron microscopy (SEM) revealed cell elongation and spreading across all samples, with more extensive presence and colonization on 008 T. This scaffold provided superior support for cell growth, making it highly suitable for bone tissue applications. Furthermore, the HIPE resin with 0.08 wt% tartrazine was successfully used to 3D print human trabecular bone structures based on microCT images, effectively supporting the growth and migration of MG-63 cells.

#### Data availability statement

All data that support the findings of this study are included within the article (and any supplementary files).

#### Acknowledgment

The authors acknowledge the Engineering and Physical Sciences Research Council (Grant No. EP/I007695/1) and the Medical Research Council (Grant No. MR/L012669/1) for funding the equipment used in this study. F C also thanks the Royal Society for funding a Royal Society Leverhulme Trust Senior Research Fellowship 2022 (SRF\R1\221053).

#### Conflict of interest

The authors declare no conflict of interest.

#### ORCID iDs

Nihan Sengokmen-Ozsoz  <https://orcid.org/0000-0002-2000-7408>

Mina Aleemardani  <https://orcid.org/0000-0001-8261-4046>

Marco Palanca  <https://orcid.org/0000-0002-1231-2728>

Gwendolen C Reilly  <https://orcid.org/0000-0003-1456-1071>

Enrico Dall'Ara  <https://orcid.org/0000-0003-1471-5077>

Frederik Claeysens  <https://orcid.org/0000-0002-1030-939X>

#### References

- [1] Owen R, Sherborne C, Paterson T, Green N H, Reilly G C and Claeysens F 2016 Emulsion templated scaffolds with tunable mechanical properties for bone tissue engineering *J. Mech. Behav. Biomed. Mater.* **54** 159–72
- [2] Malayeri A, Sherborne C, Paterson T, Mittar S, Asencio I O, Hatton P V and Claeysens F 2016 Osteosarcoma growth on trabecular bone mimicking structures manufactured via laser direct write *Int. J. Bioprint.* **2** 67–77
- [3] Wang A J, Paterson T, Owen R, Sherborne C, Dugan J, Li J M and Claeysens F 2016 Photocurable high internal phase emulsions (HIPEs) containing hydroxyapatite for additive manufacture of tissue engineering scaffolds with multi-scale porosity *Mater. Sci. Eng. C* **67** 51–58
- [4] Aldemir Dikici B, Sherborne C, Reilly G C and Claeysens F 2019 Emulsion templated scaffolds manufactured from photocurable polycaprolactone *Polymer* **175** 243–54
- [5] Dikici B A, Dikici S, Reilly G C, MacNeil S and Claeysens F 2019 A novel bilayer polycaprolactone membrane for guided bone regeneration: combining electrospinning and emulsion templating *Materials* **12** 2643
- [6] Aldemir Dikici B, Reilly G C and Claeysens F 2020 Boosting the osteogenic and angiogenic performance of multiscale porous polycaprolactone scaffolds by *in vitro* generated extracellular matrix decoration *ACS Appl. Mater. Interfaces* **12** 12510–24
- [7] Christenson E M, Soofi W, Holm J L, Cameron N R and Mikos A G 2007 Biodegradable fumarate-based polyHIPEs as tissue engineering scaffolds *Biomacromolecules* **8** 3806–14
- [8] Akay G, Birch M A and Bokhari M A 2004 Microcellular polyHIPE polymer supports osteoblast growth and bone formation *in vitro* *Biomaterials* **25** 3991–4000
- [9] Berezovska I, Kapilov K, Dhavalikar P, Cosgriff-Hernandez E and Silverstein M S 2021 Reactive surfactants for achieving open-cell poly HIPE foams from pickering emulsions *Macromol. Mater. Eng.* **306** 2000825
- [10] Durgut E, Sherborne C, Aldemir Dikici B, Reilly G C and Claeysens F 2022 Preparation of interconnected pickering polymerized high internal phase emulsions by arrested coalescence *Langmuir* **38** 10953–62
- [11] Durgut E, Zhou M, Dikici B A, Foudazi R and Claeysens F 2024 Modifying pickering polymerized high internal phase emulsion morphology by adjusting particle hydrophilicity *Colloids Surf. A* **680** 132629
- [12] Silverstein M S 2014 PolyHIPEs: recent advances in emulsion-templated porous polymers *Prog. Polym. Sci.* **39** 199–234
- [13] Sherborne C, Owen R, Reilly G C and Claeysens F 2018 Light-based additive manufacturing of PolyHIPEs: controlling the surface porosity for 3D cell culture applications *Mater. Des.* **156** 494–503

- [14] Aldemir Dikici B and Claeysens F 2020 Basic principles of emulsion templating and its use as an emerging manufacturing method of tissue engineering scaffolds *Front. Bioeng. Biotechnol.* **8** 554312
- [15] Kramer S, Cameron N R and Krajnc P 2021 Porous polymers from high internal phase emulsions as scaffolds for biological applications *Polymers* **13** 1–24
- [16] Bokhari M, Carnachan R J, Cameron N R and Przyborski S A 2007 Novel cell culture device enabling three-dimensional cell growth and improved cell function *Biochem. Biophys. Res. Commun.* **354** 1095–100
- [17] Bokhari M, Carnachan R J, Cameron N R and Przyborski S A 2007 Culture of HepG2 liver cells on three dimensional polystyrene scaffolds enhances cell structure and function during toxicological challenge *J. Anat.* **211** 567–76
- [18] REPROCELL Brand: Alvetex® (available at: [www.reprocell.com/alvetex](http://www.reprocell.com/alvetex)) (Accessed 28 October 2024)
- [19] Bokhari M, Birch M and Akay G 2003 Polyhipe polymer: a novel scaffold for *in vitro* bone tissue engineering *Adv. Exp. Med. Biol.* **534** 247–54
- [20] Hayman M W, Smith K H, Cameron N R and Przyborski S A 2004 Enhanced neurite outgrowth by human neurons grown on solid three-dimensional scaffolds *Biochem. Biophys. Res. Commun.* **314** 483–8
- [21] Naranda J, Sušec M, Maver U, Gradišnik L, Gorenjak M, Vukasović A, Ivković A, Rupnik M S, Vogrin M and Krajnc P 2016 Polyester type polyHIPE scaffolds with an interconnected porous structure for cartilage regeneration *Sci. Rep.* **6** 1–11
- [22] Richardson S A, Rawlings T M, Muter J, Walker M, Brosens J J, Cameron N R and Eissa A M 2019 Covalent attachment of fibronectin onto emulsion-templated porous polymer scaffolds enhances human endometrial stromal cell adhesion, infiltration, and function *Macromol. Biosci.* **19** 1800351
- [23] Ratcliffe J L, Walker M, Eissa A M, Du S, Przyborski S A, Laslett A L and Cameron N R 2019 Optimized peptide functionalization of thiol-acrylate emulsion-templated porous polymers leads to expansion of human pluripotent stem cells in 3D culture *J. Polym. Sci. A* **57** 1974–81
- [24] Johnson D W, Langford C R, Didsbury M P, Lipp B, Przyborski S A and Cameron N R 2015 Fully biodegradable and biocompatible emulsion templated polymer scaffolds by thiol-acrylate polymerization of polycaprolactone macromonomers *Polym. Chem.* **6** 7256–63
- [25] Lumelsky Y, Lalush-Michael I, Levenberg S and Silverstein M S 2009 A degradable, porous, emulsion-templated polyacrylate *J. Polym. Sci. A* **47** 7043–53
- [26] Changotade S, Radu Bostan G, Consalus A, Poirier F, Peltzer J, Lataillade J J, Lutomski D and Rohman G 2015 Preliminary *in vitro* assessment of stem cell compatibility with cross-linked poly( $\epsilon$ -caprolactone urethane) scaffolds designed through high internal phase emulsions *Stem Cells Int.* **2015** 283796
- [27] Hu Y, Han W, Chen Y, Zou R, Ouyang Y, Zhou W, Yang Z and Wang C 2017 One-pot fabrication of poly( $\epsilon$ -Caprolactone)-incorporated bovine serum albumin/calcium alginate/hydroxyapatite nanocomposite scaffolds by high internal phase emulsion templates *Macromol. Mater. Eng.* **302** 1600367
- [28] Hu Y, Gu X, Yang Y, Huang J, Hu M, Chen W, Tong Z and Wang C 2014 Facile fabrication of poly(l-lactic acid)-grafted hydroxyapatite/poly(lactic-co-glycolic acid) scaffolds by pickering high internal phase emulsion templates *ACS Appl. Mater. Interfaces* **6** 17166–75
- [29] Ng J Y, Obuobi S, Chua M L, Zhang C, Hong S, Kumar Y, Gokhale R and Ee P L R 2020 Biomimicry of microbial polysaccharide hydrogels for tissue engineering and regenerative medicine—a review *Carbohydrate Polym.* **241** 116345
- [30] Diekjürgen D and Grainger D W 2017 Polysaccharide matrices used in 3D *in vitro* cell culture systems *Biomaterials* **141** 96–115
- [31] Barbetta A, Massimi M, Devirgiliis L C and Dentini M 2006 Enzymatic cross-linking versus radical polymerization in the preparation of gelatin polyHIPEs and their performance as scaffolds in the culture of hepatocytes *Biomacromolecules* **7** 3059–68
- [32] Mu X, Bertron T, Dunn C, Qiao H, Wu J, Zhao Z, Saldana C and Qi H J 2017 Porous polymeric materials by 3D printing of photocurable resin *Mater. Horizons* **4** 442–9
- [33] Sears N A, Dhavalikar P S and Cosgriff-Hernandez E M 2016 Emulsion inks for 3D printing of high porosity materials *Macromol. Rapid Commun.* **37** 1369–74
- [34] Johnson D W et al 2013 Macrostructuring of emulsion-templated porous polymers by 3D laser patterning *Adv. Mater.* **25** 3178–81
- [35] Sears N, Dhavalikar P, Whitely M and Cosgriff-Hernandez E 2017 Fabrication of biomimetic bone grafts with multi-material 3D printing *Biofabrication* **9** 25020
- [36] Sengokmen Ozsoz N, Pashneh-Tala S and Claeysens F 2023 Optimization of a high internal phase emulsion-based resin for use in commercial vat photopolymerization additive manufacturing *3D Print. Addit. Manuf.* **11** 496–507
- [37] Choi J W, Wicker R B, Cho S H, Ha C S and Lee S H 2009 Cure depth control for complex 3D microstructure fabrication in dynamic mask projection microstereolithography *Rapid Prototyp. J.* **15** 59–70
- [38] Sengokmen-Ozsoz N, Boston R and Claeysens F 2023 Investigating the potential of electroless nickel plating for fabricating ultra-porous metal-based lattice structures using PolyHIPE templates *ACS Appl. Mater. Interfaces* **15** 30769–79
- [39] Maksoud F J, de la Paz Velázquez M F, Hann A J, Thanarak J, Reilly G C, Claeysens F, Green N H and Zhang Y S 2022 Porous biomaterials for tissue engineering: a review *J. Mater. Chem. B* **10** 8111–65
- [40] Liu T, Wang Y and Kuang T 2024 Oriented porous polymer scaffolds in tissue engineering: a comprehensive review of preparation strategies and applications *Macromol. Mater. Eng.* **309** 2300246
- [41] Flores-Jiménez M S, Garcia-Gonzalez A and Fuentes-Aguilar R Q 2023 Review on porous scaffolds generation process: a tissue engineering approach *ACS Appl. Bio Mater.* **6** 1–23
- [42] Oftadeh R, Perez-Viloria M, Villa-Camacho J C, Vaziri A and Nazarian A 2015 Biomechanics and mechanobiology of trabecular bone: a review *J. Biomech. Eng.* **137** 0108021
- [43] Hao J, Nangunoori R, Wu Y Y, Rajaraman M, Cook D, Yu A, Cheng B and Shimada K 2018 Material characterization and selection for 3D-printed spine models *3D Print. Med.* **4** 1–17
- [44] Kumar N, Kumar A, Uniyal P, Ramalingaiah B, Sharma S, Goni V G, Aggarwal S, Bhadada S K and Bhushan B 2020 Mimicking high strength lightweight novel structures inspired from the trabecular bone microarchitecture *Phil. Trans. R. Soc. A* **378** 20190448
- [45] Filipowska J, Tomaszewski K A, Niedźwiedzki Ł, Walocha J A and Niedźwiedzki T 2017 The role of vasculature in bone development, regeneration and proper systemic functioning *Angiogenesis* **20** 291–302
- [46] Osterhoff G, Morgan E F, Shefelbine S J, Karim L, McNamara L M and Augat P 2016 Bone mechanical properties and changes with osteoporosis *Injury* **47** S11
- [47] Pang K-L, Ogechi Ekeuku S and Chin K-Y 2024 Decellularised natural cancellous trabecular bone scaffold in tissue engineering *Functional Bio-based Materials for Regenerative Medicine From Bench to Bedside (Part 2)* (Bentham Science Publishers) pp 191–211
- [48] Rocha A A, Thiré R M S M and Araujo A C 2023 Generating STL for forming trabecular bone structure in additive manufacturing using cell dynamics modeling *Mater. Res. Proc.* **28** 169–78
- [49] Xiong Z, Rouquier L, Huang X, Potier E, Bensidhoum M and Hoc T 2024 Porosity and surface curvature effects on the permeability and wall shear stress of trabecular bone: guidelines for biomimetic scaffolds for bone repair *Comput. Biol. Med.* **177** 108630

- [50] Xiao J, Liu D, Cheng H, Jia Y, Zhou S and Zu M 2020 Carbon nanotubes as light absorbers in digital light processing three-dimensional printing of SiCN ceramics from preceramic polysilazane *Ceram. Int.* **46** 19393–400
- [51] Kolb C, Lindemann N, Wolter H and SEXTL G 2021 3D-printing of highly translucent ORMOCER<sup>®</sup>-based resin using light absorber for high dimensional accuracy *J. Appl. Polym. Sci.* **138** 49691
- [52] Zhao J, Li Q, Jin F and He N 2021 Digital light processing 3D printing Kevlar composites based on dual curing resin *Addit. Manuf.* **41** 101962
- [53] He Y, Li N, Xiang Z, Rong Y, Zhu L and Huang X 2022 Natural polyphenol as radical inhibitors used for DLP-based 3D printing of photosensitive gels *Mater. Today Commun.* **33** 104698
- [54] Narupai B, Wong J, Sanchez-Rexach E, Smith-Jones J, Le V C T, Sadaba N, Sardon H and Nelson A 2023 3D printing of ionic liquid polymer networks for stretchable conductive sensors *Adv. Mater. Technol.* **8** 2300226
- [55] Elegoo Mars 3 Pro (available at: [www.elegoo.com/products/elegoo-mars-3-pro-4k-mono-lcd-3d-printer?srsltid=AfmBOooLYDhHYj3rgwwXvtnV4GHc71bbUDxXz8dUZFAdaNzPXqpXVSG\\_](http://www.elegoo.com/products/elegoo-mars-3-pro-4k-mono-lcd-3d-printer?srsltid=AfmBOooLYDhHYj3rgwwXvtnV4GHc71bbUDxXz8dUZFAdaNzPXqpXVSG_)) (Accessed 28 October 2024)
- [56] Costa M C, Campello L B B, Ryan M, Rochester J, Viceconti M and Dall'Ara E 2020 Effect of size and location of simulated lytic lesions on the structural properties of human vertebral bodies, a micro-finite element study *Bone Rep.* **12** 100257
- [57] Palanca M, Cavazzoni G and Dall'Ara E 2023 The role of bone metastases on the mechanical competence of human vertebrae *Bone* **173** 116814
- [58] Cavazzoni G, Cristofolini L, Dall'Ara E and Palanca M 2023 Bone metastases do not affect the measurement uncertainties of a global digital volume correlation algorithm *Front. Bioeng. Biotechnol.* **11** 1152358
- [59] Barbetta A and Cameron N R 2004 Morphology and surface area of emulsion-derived (PolyHIPE) solid foams prepared with oil-phase soluble porogenic solvents: three-component surfactant system *Macromolecules* **37** 3202–13
- [60] Qu H, Fu H, Han Z and Sun Y 2019 Biomaterials for bone tissue engineering scaffolds: a review *RSC Adv.* **9** 26252–62
- [61] Roseti L, Parisi V, Petretta M, Cavallo C, Desando G, Bartolotti I and Grigolo B 2017 Scaffolds for bone tissue engineering: state of the art and new perspectives *Mater. Sci. Eng. C* **78** 1246–62
- [62] Koons G L, Diba M and Mikos A G 2020 Materials design for bone-tissue engineering *Nat. Rev. Mater.* **5** 584–603
- [63] Owen R, Sherborne C, Evans R, Reilly G C and Claeysens F 2020 Combined porogen leaching and emulsion templating to produce bone tissue engineering scaffolds *Int. J. Bioprint.* **6** 265
- [64] Murphy C M, Haugh M G and O'Brien F J 2010 The effect of mean pore size on cell attachment, proliferation and migration in collagen–glycosaminoglycan scaffolds for bone tissue engineering *Biomaterials* **31** 461–6
- [65] Hannink G and Arts J J C 2011 Bioresorbability, porosity and mechanical strength of bone substitutes: what is optimal for bone regeneration? *Injury* **42** S22–5
- [66] Abbasi N, Hamlet S, Love R M and Nguyen N T 2020 Porous scaffolds for bone regeneration *J. Sci. Adv. Mater. Devices* **5** 1–9
- [67] Aleemardani M, Johnson L, Trikić M Z, Green N H and Claeysens F 2023 Synthesis and characterisation of photocurable poly(glycerol sebacate)-co-poly(ethylene glycol) methacrylates *Mater. Today Adv.* **19** 100410
- [68] Zhang Q, Dong H, Li Y, Zhu Y, Zeng L, Gao H, Yuan B, Chen X and Mao C 2015 Microgrooved polymer substrates promote collective cell migration to accelerate fracture healing in an *in vitro* model *ACS Appl. Mater. Interfaces* **7** 23336–45
- [69] Aldemir Dikici B et al 2022 Thiolene-and polycaprolactone methacrylate-based polymerized high internal phase emulsion (PolyHIPE) scaffolds for tissue engineering *Biomacromolecules* **23** 720–30
- [70] Holzapfel B M, Reichert J C, Schantz J T, Gbureck U, Rackwitz L, Nöth U, Jakob F, Rudert M, Groll J and Hutmacher D W 2013 How smart do biomaterials need to be? A translational science and clinical point of view *Adv. Drug Deliv. Rev.* **65** 581–603
- [71] Kuboki Y, Takita H, Kobayashi D, Tsuruga E, Inoue M, Murata M, Nagai N, Dohi Y and Ohgushi H 1998 BMP-induced osteogenesis on the surface of hydroxyapatite with geometrically feasible and nonfeasible structures: topology of osteogenesis *J. Biomed. Mater. Res.* **39** 190–9
- [72] Aleemardani M, Solouk A, Akbari S, Dehghan M M and Moeini M 2020 Silk-derived oxygen-generating electrospun patches for enhancing tissue regeneration: investigation of calcium peroxide role and its effects on controlled oxygen delivery *Materialia* **14** 100877
- [73] Cidonio G, Costantini M, Pierini F, Scognamiglio C, Agarwal T and Barbetta A 2021 3D printing of biphasic inks: beyond single-scale architectural control *J. Mater. Chem. C* **9** 12489–508
- [74] Kuboki Y, Jin Q, Kikuchi M, Mamood J and Takita H 2009 Geometry of artificial ECM: sizes of pores controlling phenotype expression in BMP-induced osteogenesis and chondrogenesis *Connect. Tissue Res.* **43** 529–34
- [75] Paterson T 2017 PolyHIPE microspheres for injectable bone tissue engineering applications *PhD Thesis* The University of Sheffield
- [76] Paterson T E, Sherborne C, Green N H, Claeysens F, Reilly G C, MacNeil S, Dugan J M and Gigliobianco G 2018 Porous microspheres support mesenchymal progenitor cell ingrowth and stimulate angiogenesis *APL Bioeng.* **2** 026103
- [77] Barak M M and Black M A 2018 A novel use of 3D printing model demonstrates the effects of deteriorated trabecular bone structure on bone stiffness and strength *J. Mech. Behav. Biomed. Mater.* **78** 455–64
- [78] Grzeszczak A, Lewin S, Eriksson O, Kreuger J and Persson C 2021 The potential of stereolithography for 3D printing of synthetic trabecular bone structures *Materials* **14** 3712
- [79] Chesnais F, Joel J, Hue J, Shakib S, Di Silvio L, Grigoriadis A E, Coward T and Veschini L 2023 Continuously perfusable, customisable, and matrix-free vasculature on a chip platform † *Lab Chip* **23** 761
- [80] Kalantari S M, Arabi H, Mirdamadi S and Mirsalehi S A 2015 Biocompatibility and compressive properties of Ti-6Al-4V scaffolds having Mg element *J. Mech. Behav. Biomed. Mater.* **48** 183–91
- [81] Misra S K, Ansari T I, Valappil S P, Mohn D, Philip S E, Stark W J, Roy I, Knowles J C, Salih V and Boccaccini A R 2010 Poly(3-hydroxybutyrate) multifunctional composite scaffolds for tissue engineering applications *Biomaterials* **31** 2806–15
- [82] Gao C, Liu T, Shuai C and Peng S 2014 Enhancement mechanisms of graphene in nano-58S bioactive glass scaffold: mechanical and biological performance *Sci. Rep.* **4** 1–10
- [83] Stadelmann M A, Schenk D E, Maquer G, Lenherr C, Buck F M, Bosshardt D D, Hoppe S, Theumann N, Alkalay R N and Zysset P K 2020 Conventional finite element models estimate the strength of metastatic human vertebrae despite alterations of the bone's tissue and structure *Bone* **141** 115598
- [84] Jadzic J, Cvetkovic D, Milovanovic P, Tomanovic N, Zivkovic V, Nikolic S, Djuric M and Djonic D 2020 The micro-structural analysis of lumbar vertebrae in alcoholic liver cirrhosis *Osteoporos. Int.* **31** 2209–17
- [85] Ryan M, Barnett L, Rochester J, Wilkinson J M and Dall'Ara E 2020 A new approach to comprehensively evaluate the morphological properties of the human femoral head: example of application to osteoarthritic joint *Sci. Rep.* **10** 5538